

The Basins of Attraction of Soft Sphere Packings Are Not Fractal

Praharsh Suryadevara,^{1,*} Mathias Casiulis,^{1,2,*} and Stefano Martiniani^{1,2,3,4,†}

¹*Center for Soft Matter Research, Department of Physics, New York University, New York 10003, USA*

²*Simons Center for Computational Physical Chemistry, Department of Chemistry, New York University, New York 10003, USA*

³*Courant Institute of Mathematical Sciences, New York University, New York 10003, USA*

⁴*Center for Neural Science, New York University, New York 10003, USA*

(Dated: July 8, 2025)

The energy landscape plays a central role in understanding the dynamics of low-temperature and athermal systems, which are characterized by a plethora of minima and the intricate geometry of their basins of attraction. Due to their complexity, these landscapes resist analytical treatment and must instead be studied numerically. We focus on jammed soft spheres, a paradigmatic model of glasses and granulars, to expose the limitations of standard numerical methods in resolving the true structure energy landscapes. We show that CVODE is the ODE solver with the best time-for-error trade-off, outperforming commonly used steepest-descent solvers by several orders of magnitude. Using this numerical approach, we provide unequivocal evidence that optimizers widely used in computational studies of soft sphere packings destroy all semblance of the true landscape geometry, even in moderately low dimensions. Employing a range of geometric indicators, both low- and high-dimensional, we show that earlier claims on the fractality of basins of attraction originated from the use of inadequate mapping strategies. In reality, the basins of attraction of soft sphere packings are smooth structures with well-defined length scales.

The energy landscape framework, which maps the configuration of a system of N particles interacting through conservative forces in d dimensions to a single point on a dN -dimensional potential energy surface, is a central tool in the study of many-body systems [1]. In glassy systems, mean-field theories predict that the (free) energy landscape is characteristically rough, giving rise to rich physical behavior [2–5]. In two and three dimensions, however, analytical theories are out of reach, making numerical investigations indispensable. A substantial body of work has thus focused on the landscape of computer-simulated soft sphere packings [6–22]. Quantities of interest include the (combinatorially large) number of low-lying minima [3, 7, 10, 22–24], and the probabilities of finding states near each of these minima—both linked to the configurational entropy [10, 13, 15, 17, 25–28]. These properties can be probed by studying the *basins of attraction* [1], the sets of points linked to each minimum by a path of steepest descent. This path describes dynamics after instantaneous quenches to zero temperature, making basin volumes a measurement of configurational entropy [10, 13, 15], while their relative arrangement governs relaxation pathways [21].

Characterizing basins of attraction is notoriously difficult due to the high dimensionality of configuration space, dN . In high dimensions, even simple geometric objects like hypercubes are costly to measure, as their volume concentrates in a thin layer, deep into the exponentially many narrow corners [29, 30]. Basins of attraction are typically far more complex, exhibiting non-trivial, non-convex geometries [16, 26] (Fig. 1 and video in SM [31]), but these geometric intricacies are only one aspect of the numerical challenge posed by measuring basins of attraction.

Determining whether a given point lies inside a basin

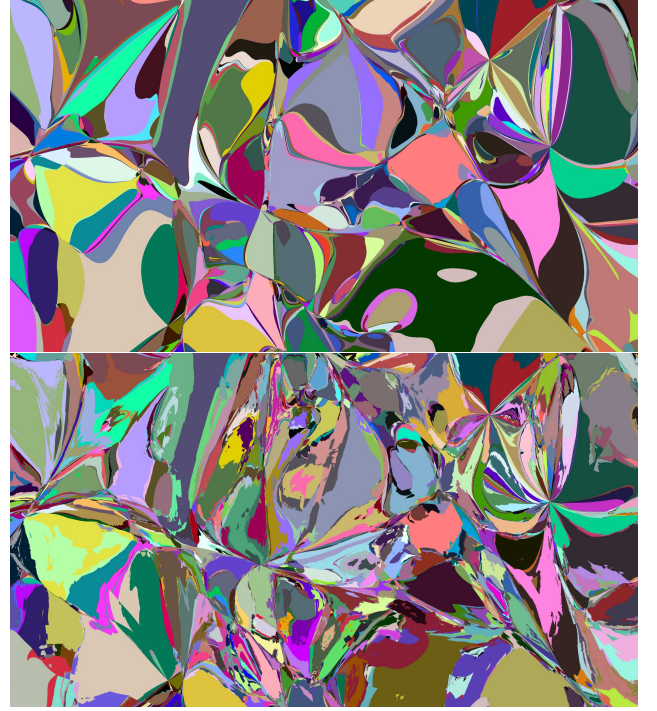


FIG. 1. **Slicing the energy landscape.** A random $2d$ plane is selected in the configuration space of $N = 16$ disks, 1350×2400 pixels are drawn along that plane. At each pixel, we use CVODE (top) and FIRE (bottom), to identify which basin of attraction it belongs to. Each basin is uniquely encoded by one color across both panels.

requires integrating the steepest-descent ordinary differential equation (ODE) in dN dimensions. In soft spheres close to jamming, the landscape exhibits nearly flat directions around minima, leading to ill-conditioned Hes-

sians and stiff ODEs. As integrating such ODEs accurately is computationally intensive, most prior work adopted heuristic optimizers to perform energy quenches, either momentum-based methods like FIRE [32] or quasi-Newton schemes like L-BFGS [33].

In this paper, using a fast yet accurate ODE solver with adaptive stepsize control, we show that optimizers destroy geometric features of the energy landscape of systems of soft particles in $d = 2$, even at moderate N (Fig. 1), so much so that for $N \gtrsim 64$ these algorithms essentially *never* map an initial point to the right minimum. Using several quantitative measures of the geometry of basins, we show that optimizer-based relaxations create a mirage: basins appear to exhibit fractal structure and a scale-free distribution of sizes. Adequate numerical methods reveal that both impressions are wrong. In particular, normalizing the basin density of states by that of a hypersphere [16] (i.e., accurately measuring the probability of ball-picking inside the basin by importance sampling), we find exponential, not power-law, decays – directly demonstrating that the basins of jammed soft spheres are not fractal. Finally, we show that using optimizers to estimate basin volumes [10, 15, 22, 34] introduces a systematic bias that grows with N , suggesting that past estimates of the number of minima in potential energy landscapes (e.g. [10, 13, 16]) are biased, even though their qualitative scaling seemingly remain valid.

Model – We focus on a two-dimensional polydisperse collection of N particles in a periodic square with side-length L interacting via a Hertzian repulsive potential,

$$V_{ij}(r_{ij}) = \left(1 - \frac{r_{ij}}{R_i + R_j}\right)^{5/2} \mathbb{1}(r \leq R_i + R_j). \quad (1)$$

Here R_i is the radius of particle i , r_{ij} is the metric distance between the centers of particles i and j , and $\mathbb{1}$ is an indicator function. Half the radii are positive-normal distributed with mean $\mu_s = 1.0$ and standard deviation $\sigma_s = 0.05$, and the other half with $\mu_\ell = 1.4$ and $\sigma_\ell = 0.07$. This choice ensures that particles do not crystallize and that minima of the energy are not connected by permutation symmetry [10, 34]. Due to periodic boundary conditions, the energy $E = \sum_{i < j} V_{ij}$ is invariant by translation in d directions, so that only $(N - 1)d$ degrees of freedom persist. Introducing the packing fraction $\phi = \pi \sum_{i=1}^N R_i^2 / L^2$, the system undergoes a jamming transition at $\phi_J \approx 0.84$ [35], see Appendix. For $\phi < \phi_J$, the energy is minimized in flat regions with $E = 0$, or liquid states, where all contacts between particles can be removed at no energy cost. For $\phi \geq \phi_J$, however, most minima of the energy comprise a backbone of particles that are collectively stuck in place, such that displacing any backbone particle increases E , and only a few *rattlers* remain free to move without affecting the energy. Unless otherwise specified, we henceforth work exclusively at $\phi = 0.9$, far from ϕ_J .

Unscrambling the energy landscape – We benchmark common ODE solvers for Hertzian disks [31, 36, 37], and find that the best time-for-error is achieved by the CVODE solver [38, 39]. Note that all ODE solvers converge to the same relaxation trajectories at small tolerances, and that CVODE performs well in potentials other than Hertzian repulsion [31]. For each set (N, ϕ) , we tighten the tolerance of CVODE until the minima associated with a collection of random points in configuration space stop changing [31]. Armed with this fast, accurate map of configuration space, we measure how much error is introduced by using optimizers to identify basins.

In Fig. 1 we show the same random $2d$ slice of configuration space, where each pixel on a grid is used as an initial condition for steepest descent and each basin is represented by a unique color, using CVODE and FIRE [32], the most widely used optimizer in jammed systems [17, 19, 22, 40–42]. Here, we use a strictly downhill variant of FIRE with limited stepsize [13, 31]. Minima are matched across the two slices based on the metric distance between their locations (after rattler removal [31]). Fig. 1 shows that, even in moderate dimension, $(N - 1)d = 30$, FIRE scrambles the basins, creates discontinuities in their shapes, and alters their sizes. The apparent roughness of basins in similar $2d$ cuts has been argued to be a feature of basins, and an indicator of the fractal nature of their geometry [6, 12, 43] (not to be confused with claims of fractality of the arrangement of basins in a Gardner phase, [3, 19, 44], or of relaxation paths [14, 21]). We show that these features are in fact artifacts of inaccurate noiseless relaxations, that map points to the wrong basins of attraction.

To be more quantitative, in Fig. 2, we consider ensembles of independent random points drawn from the configuration space of collections of Hertzian disks with $N \in [8; 4096]$. In panel (a), we report the accuracy, i.e. the fraction of points that are mapped to the right minimum, against N across methods, with the ground truth given by low-tolerance CVODE ($\text{rtol} = 10^{-14}$, see SM [31]). The points reported for CVODE are obtained using a tolerance ten times looser than the ground truth reference [31], showing that it retains high accuracy. While FIRE and L-BFGS are relatively accurate for $(N - 1)d \lesssim 10$ [12], their accuracies fall exponentially with N (dashed lines), dropping near zero for $N \gtrsim 64$. Thus, for systems with more than a few tens of particles, optimizers practically *never* map a point in configurational space to the right basin of attraction. We also test an adaptive Gradient Descent algorithm [31, 46] with 2 choices of the parameter ϵ that sets the stepsize. If ϵ is fixed (GD), accuracy also falls (like a stretched exponential), and approaches zero for $N > 128$ for the ϵ used in Ref. 46. We also show that ϵ may be set at each N to achieve 98% accuracy (GD98)—at a significant time cost. This is shown in panel (b), where we plot the corresponding wall times against N , in log-log

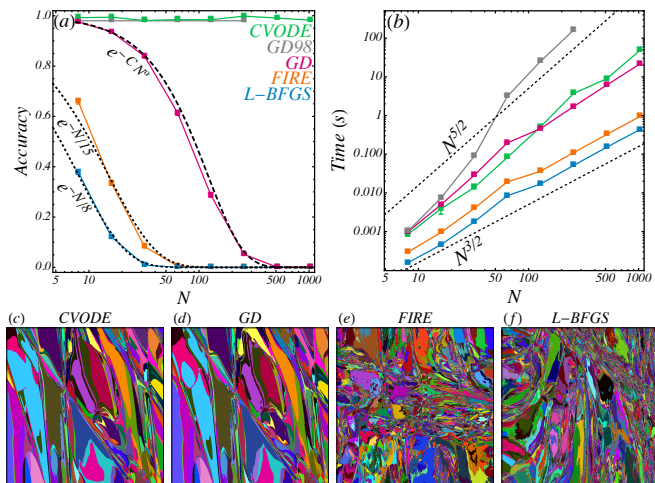


FIG. 2. **Optimizers: fast but inaccurate.** (a) Average accuracy of algorithms compared to low-tolerance CVODE, computed over 10^4 random uniform initial conditions. Error bars are Clopper-Pearson 95% confidence intervals [31, 45]. Dashed lines are exponential fits, and the long-dashed line is a stretched exponential fit. (b) Corresponding scalings of the average computation times, with error bars showing Student-T 95% confidence intervals [31]. (c) – (e) The same method as in Fig. 1 is applied to a 800×800 pixels slice for $N = 128$ particles for (c) CVODE, (d) GD, (e) FIRE, and (f) L-BFGS.

scale. While CVODE is slower than FIRE and L-BFGS ($\mathcal{O}(N^{5/2})$ vs. $\mathcal{O}(N^{3/2})$), it achieves computation times much smaller than GD98 with better accuracy (CVODE times are comparable to GD ones). To complete this picture, we show in Fig. 2(c) – (f) slices obtained like in Fig. 1, but this time at $N = 128$, where the accuracies of FIRE and L-BFGS are essentially zero. These slices reveal a much starker contrast between methods than Fig. 1, as FIRE and L-BFGS turn the whole landscape into an unrecognizable collection of confetti-like, largely disconnected basins. In fact, *not a single pixel* of the slices obtained with these optimizers falls into the right basin. The GD slice still looks reasonably smooth, but displays large regions of incorrectly tagged basins. Note the timescales involved in CVODE, that reach *minutes per minimization* in the systems we consider: quenches in Fig. 2(c) took 3 weeks of CPU time, *vs.* 3 hours for Fig. 2(e).

This first set of results has far-reaching consequences. Save from the few studies that considered very small systems (*e.g.* [10–12, 34, 47]), the vast majority of past works likely misattributed every single basin. In particular, using an accurate GD requires unreasonable computation times for such a stiff problem.

Interestingly, the distribution of minimum energies found starting from uniform random initial condition is also altered, see Appendix. Optimizers systematically bias the mean energy towards lower values by a growing, yet subextensive amount, so that the error on the

energy per particle vanishes very slowly, as $N^{-1/6}$. For Hertzian disks, the prefactor is small enough that the relative error is always within a few percent, but other potentials may display larger errors with equally slow vanishing rate. Furthermore, this bias also affects estimates of the location of the jamming point in finite size systems, with an error that vanishes slower than $N^{-1/3}$.

Low-dimensional geometric features – To give concrete examples of the effects of numerical inaccuracy in identifying basins, we now turn our attention to the geometry of basins [16]. First, we study a simple low-dimensional signature of the geometry of basins. By analogy with Fig. 1, we spawn random segments in configuration space, and use pixels on that segment as initial conditions for minimization. We then tag each pixel by the basin it falls into and measure the (discretized) intersection lengths ℓ_{ij} of segment i with each distinct basin j that it crossed. The resulting empirical distribution $p(\ell)$ across a collection of random segments is shown in Fig. 3(a), for CVODE and L-BFGS, in log-log scale. We report that $p(\ell)$, while it retains a power-law-looking decay across methods, looks very different between CVODE and L-BFGS measurements. Indeed, L-BFGS overestimates the amount of small basins, and thus overestimates the decay exponent of the distribution, as expected from the “confetti” picture, Fig. 2(c) – (f).

We now take advantage of the precision afforded by CVODE to investigate the true distribution of line intersections. Since the true distribution of ℓ is very broad, one would need an enormous amount of regularly-spaced points on lines to avoid being resolution limited. To bypass this limitation, in all sampled segments, at every observed boundary between two basins, we produce new segments with a finer resolution. Furthermore, since the distribution is broad, we focus on the distribution of the

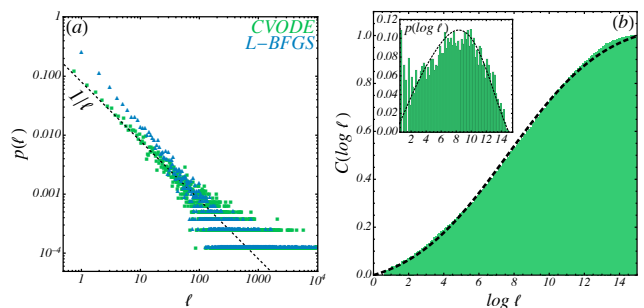


FIG. 3. **Linear intersects of basins.** (a) Intersection lengths distributions obtained with L-BFGS (blue triangles) and CVODE (green squares) over 10 lines of 10^6 pixels for $N = 16$, in log scales. A dashed line indicates $1/\ell$ behavior. (b) CDF of the distribution of $\log \ell$ obtained with CVODE by zooming $100\times$ on each basin boundary found from panel (a). The dashed black line is a truncated Gaussian fit. Inset: Corresponding histogram of the pdf, the dashed line shows a kernel regression.

logarithm of lengths, $p(\log \ell)$.

The resulting distribution is shown in Fig. 3(b). We find that the distribution of log-lengths is normal, indicating that lengths are log-normal distributed. This connects well with prior results on basin volumes of soft sphere packings, which have been argued to be log-normal distributed both from numerical measurements [13, 16, 48] and theoretical arguments [49]. Indeed, consistently with our observation that intersection lengths are log-normal distributed, the volume of the intersection of a basin with an n -dimensional affine space may be approximated by a product of n independent log-normal lengths, which yields a log-normal distribution of volumes. The observation of a log-normal distribution invalidates claims that the distribution of basin intersection lengths is scale-free [50]: a power-law tail with exponent -1 is observed due to the asymptotic behavior of log-normal distributions with large variances [51]. Likewise, claims of scale-free distributions of basin volumes [22, 52] (at odds with direct numerical measurements [13, 16, 48]) likely stemmed from inadequate sampling of a log-normal distribution, of which only the tail was seen, a common issue with small sample sizes [53].

Additionally, we evaluate the box-counting dimension d_B of basins in $2d$ slices of $N = 128$ disks such as those in Fig. 2. We find (see Appendix) that the average fractal dimension of basin boundaries is significantly closer to 1 with CVODE and GD ($d_B \approx 1.1$) than it is with FIRE and L-BFGS ($d_B \approx 1.3$). Furthermore, we find that optimizers predict a growing d_B as $\phi \rightarrow \phi_J$, while the CVODE estimate remains roughly constant. In other words, optimizers do create an illusion of fractality, that grows stronger near jamming. Note that recent work showed large basins of the Random Lorentz Gas, a minimal single-particle proxy model for jamming, to be fractal [54]—it would be interesting to understand how this feature vanishes in many-body models.

Full-dimensional geometric features – We finally focus on full-dimensional geometric measurements. First, we pick a random point in the landscape, find the basin it belongs to, then measure a “survival” probability a distance away. To do so, we generate points at distance R by uniform hypersphere point-picking, then measure the fraction of points P_{in} that land back at the same minimum. The results are shown in Fig. 4(a). For $N = 1024$ particles, we use 13 reference points for CVODE and 43 points for L-BFGS and FIRE, then around each of them we sample 1000 points on each of 30 nested hyperspheres. Optimizers consistently fall out of the basin at smaller distances, even at high density ($\phi = 0.9$), to the point that L-BFGS falls out even at minute displacements. In panel (b), we perform the same measurement closer to jamming, $\phi = 0.85$ and find that both optimizers display power-law-looking decays, once again creating an impression of fractality. However, CVODE reveals a much broader region belonging to the basin, which is

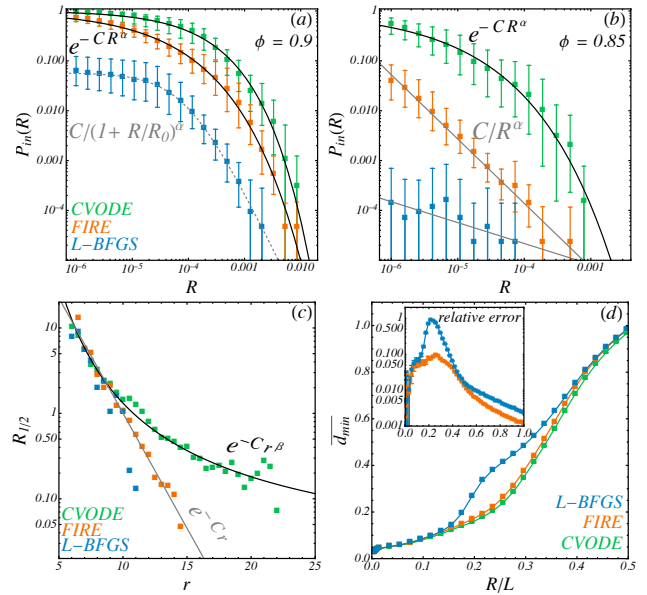


FIG. 4. Survival (a) Survival from a random point in the landscape of $N = 1024$ disks, in log-log scale. Solid black lines are stretched-exponential fits for CVODE and FIRE. Dashed gray line: saturating power-law fit to L-BFGS. Error bars are Clopper-Pearson estimates [45]. (b) Same curve at $\phi = 0.85$. Gray lines are power-law fits for FIRE and L-BFGS. The black line is a stretched-exponential fit to CVODE. (c) Half-survival radius $R_{1/2}$ inside a single basin against distance r to its minimum for $N = 128$. Lines indicate proposed fits, exponential (gray) for FIRE and L-BFGS and stretched-exponential (black) for CVODE. (d) Average distance \bar{d}_{min} between neighboring minima using kicks of size R , for $N = 1024$. Inset: log-scale relative error in \bar{d}_{min} for optimizers *vs.* CVODE.

well fitted by a stretched exponential $\exp(-Cr^\alpha)$, indicating that the basins are not scale-free by that measurement either, even close to jamming (see additional ϕ 's in SM [31]). To better characterize the shapes of basins, we perform similar survival measurements but this time centering hyperspheres on random samples within a *single basin*. We measure the distance $R_{1/2}$ at which survival first hits 1/2 as a function of the distance r between the random sample and the minimum, and thus estimate a typical cross-sectional length of the basin. Results are shown in Fig. 4(c) for $N = 128$. In this figure, we bin radial distance from the minimum into bins with width 0.1, gather 10 points per bin, and then sample 1000 points per hypersphere centered on each of these points across 15 shell radii (order 10^6 points per method). We report exponential decays with optimizers, and stretched exponential behavior for CVODE. In hypercubes, the cross-section of corners decays exponentially with distance to the center [29]. Thus, a stretched exponential indicates that basins have “thicker” tentacles than cubes, in line with observations that “tentacles” contributed to basin volumes up to large distances in sphere packings [11, 16],

Kuramoto models [26, 55], and neural networks [56].

We now study basin arrangement, following Ref. [19]. Starting from 13 random minima, we define a collection of nested hyperspheres centered on each minimum, and sample 1000 random points uniformly on each of them. We then minimize and keep a record of all new minima that are found. For each new minimum, we compute a rescaled distance to the initial minimum, d_{min} , as defined in Ref. [19] (see SM [31]), then compute its average \bar{d}_{min} as a measure of the difference between the neighborhoods of basins in each method. We show in Fig. 4(d) that for $N = 1024$, \bar{d}_{min} is significantly shifted when using optimizers, with a clear maximal deviation of 10 to 80% at intermediate hypersphere radii R . Thus, the measured basin organization is clearly affected by the choice of minimization method.

Finally, we perform basin volume measurements, using a Markov-Chain Monte-Carlo (MCMC) method [10, 13, 16, 17, 30] akin to Frenkel-Ladd measurements of free energies [57] (see SM [31]). In short, the method relies on K random walks constrained to remain in the basin of interest, each biased by a different harmonic potential centered on the minimum, and coupled to each other through Replica-Exchange Monte Carlo moves. The method estimates the free energy of each walker, and in particular that of a free walker F_0 , which is linked to the volume V of the basin via $F_0 = -\ln V$. At each MCMC step of each random walk, a full minimization is run to check whether the proposed new position still lies in the basin of interest. As a result, we expect this method to be significantly affected by the inaccuracy of optimizers. We test this hypothesis at $\phi = 0.9$ and across system sizes that remain amenable to using CVODE (recall that the MCMC takes order 10^6 steps [17, 30], and the time of a typical minimization from Fig. 2).

The results for F_0/N are shown in Fig. 5(a). We show that, while FIRE and L-BFGS yield near-indistinguishable values, there is a systematic bias between CVODE and optimizers. Worse, the systematic bias grows with system size, as FIRE and L-BFGS become more and more inaccurate. Note that the volumes measured by optimizers are *larger* than the true volumes. This counter-intuitive result is confirmed by the radial densities of states (DOS) reconstructed from samples in example basins, Fig. 5(b)–(c). Using the rescaled radial distance to the minimum $r/\sqrt{(N-1)d}$, which keeps the length of a long diagonal of a unit cube constant across dimensions, the CVODE DOS are all maximal around 1, while the FIRE ones systematically shift to higher values; indeed, FIRE finds samples lying further away from the minimum. However, in Fig. 5(d), we show the accuracy of FIRE samples obtained from the same basins as in (b)–(c) as a function of rescaled radial distance, revealing that the accuracy plummets after 0.7, with a decay that goes exponentially with distance and gets faster with dimensionality (inset). In other words, FIRE wrongly tags

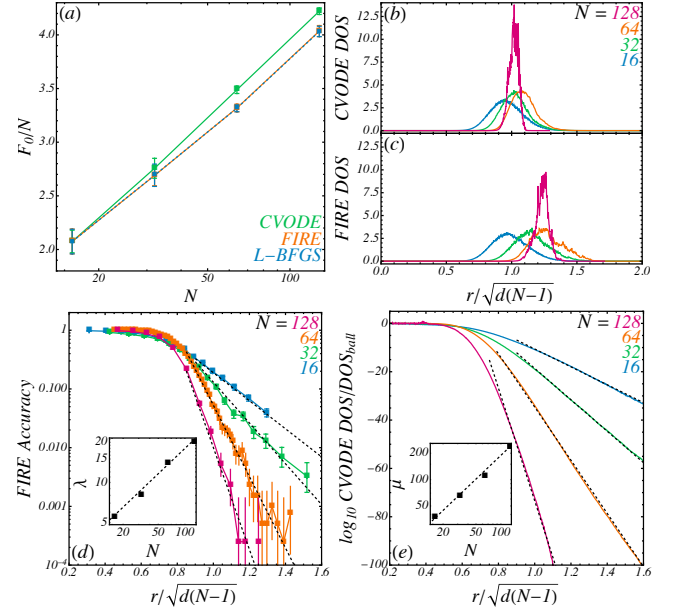


FIG. 5. **Basin volumes.** (a) Intensive free energies F_0/N across methods, against N , each averaged over the same 5 basins for each N . (b)–(c) Example densities of states (DOS) for one basin per N , for (b) CVODE, and (c) FIRE. (d) Averaged accuracy over $\mathcal{O}(10^5)$ FIRE samples used, against their distance to the minimum, in semi-log scale. Dashed lines are exponential fits $y = C \exp(-\lambda x)$ of each curve. The best decay rate λ is plotted against N in log-log in inset, with a dashed power-law $\lambda \sim N^{0.6}$. (e) \log_{10} of the ratio between the CVODE DOS of the basins in (b)–(c) and that of a hyperball in $N(d-1)$ dimensions. Dashed lines are exponential fits, and the decay rate μ is plotted against N in log-log in inset, with a dashed power-law $\mu \sim N^{0.9}$.

points outside of basins as belonging to them, likely because inertia facilitates ridge crossing. In high dimension, a slightly larger spherical shell contributes an enormous volume, so that these erroneous points lead to a systematic volume overestimate.

Finally, in Fig. 5(e), we show the DOS of the same basins, predicted by CVODE, and divided by that of a ball [16, 30]. This function measures how much sparser than a ball the basin becomes as r grows. The accuracy of FIRE samples, Fig. 5(d), starts falling at distances slightly larger than the radius of the largest inscribed ball (where curves start dropping in Fig. 5(e)), meaning that inaccuracy sets in when entering the basin “tentacles” [58]. This also explains the growing disagreement between CVODE and optimizers as N increases: in higher dimensions, the volume of the largest inscribed ball is vanishingly small [30]!

Conclusions – We uncovered a flaw that affects many works on the energy landscape of soft sphere packings, and likely of other models – that optimizers are too inaccurate to map minima and their basins of attraction, even at low dN . Having proposed CVODE as a viable ODE

solver for these problems up to $dN \sim 10^3$, we demonstrated how optimizers fail not just at assigning points to the right basin, but also at capturing simple geometric features of basins like their volumes or linear lengths. In particular, basins are not, as it has been claimed, scale-free or fractal objects in the landscape. Instead, like volumes, their geometric lengths are log-normal distributed at any given N and ϕ . Interestingly, log-normal distributions have also been reported in random sequential fragmentation processes [59–62]. Thus, configuration space splitting into an increasing number of basins of attraction as $\phi \rightarrow \phi_J$ might be interpretable as a random fragmentation process, *e.g.* as the high-dimensional crumpling of the potential energy surface.

Furthermore, we showed that full-dimensional properties of the basin, like its volume or mass repartition, are badly affected by the use of optimizers for basin identification. This affects the interpretation of notable results on jammed packings. For instance, the validity of Edwards’s conjecture, (*i.e.* that packings are equiprobable at jamming), was established using FIRE [17]. While this result holds for FIRE relaxations, a legitimate nonequilibrium protocol, it does not *a priori* reflect a property of the true energy landscape of jammed soft spheres.

Acknowledgments – The authors would like to thank Chris Rackauckas and Yingbo Ma from JuliaHub for help with benchmarking various ODE solvers. The authors would also like to thank Eric Corwin, Peter K. Morse and R. Cameron Dennis for their comprehensive feedback, as well as David Grier and John Crocker for insightful comments on this work. P.S., M.C., and S.M. acknowledge the Simons Center for Computational Physical Chemistry for financial support. This work was supported by the National Science Foundation grant IIS-2226387 and DMR-2443027. This work was supported in part through the NYU IT High Performance Computing resources, services, and staff expertise.

Contribution statement – P.S. developed the simulation code original to this paper. P.S. and M.C. performed the numerical calculations. P.S., M.C. and S.M. conceptualized the work, analyzed the data, and wrote the manuscript.

* Equal contribution.

† sm7683@nyu.edu

- [1] F. H. Stillinger, *Energy Landscapes, Inherent Structures, and Condensed-Matter Phenomena* (Princeton University Press, 2015).
- [2] G. Parisi and F. Zamponi, Mean-field theory of hard sphere glasses and jamming, *Reviews of Modern Physics* **82**, 789 (2010).
- [3] P. Charbonneau, J. Kurchan, G. Parisi, P. Urbani, and F. Zamponi, Fractal free energy landscapes in structural glasses, *Nature Communications* **5**, 4725 (2014).
- [4] G. Biroli and P. Urbani, Breakdown of elasticity in amorphous solids, *Nature Physics* **12**, 1130 (2016).
- [5] G. Foleni, S. Franz, and F. Ricci-Tersenghi, Rethinking Mean-Field Glassy Dynamics and Its Relation with the Energy Landscape: The Surprising Case of the Spherical Mixed p -Spin Model, *Physical Review X* **10**, 31045 (2020).
- [6] D. J. Wales, Basins of Attraction for Stationary Points on a Potential-Energy Surface, *Journal of the Chemical Society: Faraday Transactions* **88**, 653 (1992).
- [7] A. Heuer, Properties of a glass-forming system as derived from its potential energy landscape, *Physical Review Letters* **78**, 4051 (1997).
- [8] A. Saksangwong, B. Doliwa, and A. Heuer, Description of the dynamics in complex energy landscapes via metabasins: A simple model study, *Journal of Physics Condensed Matter* **15**, S1237 (2003).
- [9] T. V. Bogdan, D. J. Wales, and F. Calvo, Equilibrium thermodynamics from basin-sampling, *Journal of Chemical Physics* **124**, 044102 (2006).
- [10] N. Xu, D. Frenkel, and A. J. Liu, Direct determination of the size of basins of attraction of jammed solids, *Physical Review Letters* **106**, 245502 (2011).
- [11] S. S. Ashwin, J. Blawdziewicz, C. S. O’Hern, and M. D. Shattuck, Calculations of the structure of basin volumes for mechanically stable packings, *Physical Review E - Statistical, Nonlinear, and Soft Matter Physics* **85**, 061307 (2012).
- [12] D. Asenjo, J. D. Stevenson, D. J. Wales, and D. Frenkel, Visualizing basins of attraction for different minimization algorithms, *Journal of Physical Chemistry B* **117**, 12717 (2013).
- [13] D. Asenjo, F. Paillusson, and D. Frenkel, Numerical calculation of granular entropy, *Physical Review Letters* **112**, 098002 (2014).
- [14] H. J. Hwang, R. A. Riggelman, and J. C. Crocker, Understanding soft glassy materials using an energy landscape approach, *Nature Materials* **15**, 1031 (2016).
- [15] S. Martiniani, K. J. Schrenk, J. D. Stevenson, D. J. Wales, and D. Frenkel, Turning intractable counting into sampling: Computing the configurational entropy of three-dimensional jammed packings, *Physical Review E* **93**, 012906 (2016).
- [16] S. Martiniani, K. J. Schrenk, J. D. Stevenson, D. J. Wales, and D. Frenkel, Structural analysis of high-dimensional basins of attraction, *Physical Review E* **94**, 031301(R) (2016).
- [17] S. Martiniani, K. J. Schrenk, K. Ramola, B. Chakraborty, and D. Frenkel, Numerical test of the Edwards conjecture shows that all packings are equally probable at jamming, *Nature Physics* **13**, 848 (2017).
- [18] D. J. Wales, Exploring Energy Landscapes, *Annual Review of Physical Chemistry* **69**, 401 (2018).
- [19] R. C. Dennis and E. I. Corwin, Jamming Energy Landscape is Hierarchical and Ultrametric, *Physical Review Letters* **124**, 78002 (2020).
- [20] H. H. Boltz, J. Kurchan, and A. J. Liu, Fluctuation distributions of energy minima in complex landscapes, *Physical Review Research* **3**, 013061 (2021).
- [21] A. Thirumalaiswamy, R. A. Riggelman, and J. C. Crocker, Exploring canyons in glassy energy landscapes using metadynamics, *Proceedings of the National Academy of Sciences* **119**, e2210535119 (2022).
- [22] V. F. Haghighi and S. R. Nagel, Permutation Symmetry

- Restoration in Disordered Materials, Arxiv Preprint , 2403.03926 (2024), arXiv:2403.03926.
- [23] F. H. Stillinger and T. A. Weber, Hidden structure in liquids, *Physical Review A* **25**, 978 (1982).
 - [24] F. H. Stillinger and T. A. Weber, Packing structures and transitions in liquids and solids, *Science* **225**, 983 (1984).
 - [25] S. Martiniani, P. M. Chaikin, and D. Levine, Quantifying Hidden Order out of Equilibrium, *Physical Review X* **9**, 11031 (2019).
 - [26] S. Martiniani, *On the complexity of energy landscapes: algorithms and a direct test of the Edwards conjecture*, Ph.D. thesis (2017).
 - [27] F. Sciortino, W. Kob, and P. Tartaglia, Inherent structure entropy of supercooled liquids, *Physical Review Letters* **83**, 3214 (1999).
 - [28] F. Sciortino, Potential energy landscape description of supercooled liquids and glasses, *Journal of Statistical Mechanics: Theory and Experiment* **2005**, P05015 (2005).
 - [29] S. Artstein-Avidan, A. Giannopoulos, and V. D. Milman, *Asymptotic Geometric Analysis , Part I*, Vol. 202 (American Mathematical Society, Providence, Rhode Island, 2015).
 - [30] M. Casiulis and S. Martiniani, When you can't count, sample! Computable entropies beyond equilibrium from basin volumes, *Papers in Physics* **15**, 150001 (2023).
 - [31] See Supplemental Material at `URL_will_be_inserted_by_publisher` for a detailed discussion of the choice of ODE solver and of its parameters, a complete description of numerical methods, a video of slices of basins obtained by moving along a third orthogonal direction, and additional data on the effect of both N and ϕ on the landscape.
 - [32] E. Bitzek, P. Koskinen, F. Gähler, M. Moseler, and P. Gumbsch, Structural relaxation made simple, *Physical Review Letters* **97**, 170201 (2006).
 - [33] D. C. Liu and J. Nocedal, On the limited memory BFGS method for large-scale optimization, *Mathematical Programming* **45**, 503 (1989).
 - [34] G. J. Gao, J. Bławdziewicz, and C. S. O'Hern, Frequency distribution of mechanically stable disk packings, *Physical Review E - Statistical, Nonlinear, and Soft Matter Physics* **74**, 061304 (2006).
 - [35] C. S. O'Hern, L. E. Silbert, A. J. Liu, and S. R. Nagel, Jamming at zero temperature and zero applied stress: The epitome of disorder, *Physical Review E - Statistical Physics, Plasmas, Fluids, and Related Interdisciplinary Topics* **68**, 011306 (2003).
 - [36] C. Rackauckas and Q. Nie, DifferentialEquations.jl – A Performant and Feature-Rich Ecosystem for Solving Differential Equations in Julia, *Journal of Open Research Software* **5**, 15 (2017).
 - [37] C. Rackauckas and Q. Nie, Confederated modular differential equation APIs for accelerated algorithm development and benchmarking, *Advances in Engineering Software* **132**, 1 (2019).
 - [38] A. C. Hindmarsh, P. N. Brown, K. E. Grant, S. L. Lee, R. Serban, D. E. Shumaker, and C. S. Woodward, SUNDIALS: Suite of nonlinear and differential/algebraic equation solvers, *ACM Transactions on Mathematical Software* **31**, 363 (2005).
 - [39] D. J. Gardner, D. R. Reynolds, C. S. Woodward, and C. J. Balos, Enabling New Flexibility in the SUNDIALS Suite of Nonlinear and Differential/Algebraic Equation Solvers, *ACM Transactions on Mathematical Software* **48**, 31 (2022).
 - [40] C. P. Goodrich, S. Dagois-Bohy, B. P. Tighe, M. Van Hecke, A. J. Liu, and S. R. Nagel, Jamming in finite systems: Stability, anisotropy, fluctuations, and scaling, *Physical Review E - Statistical, Nonlinear, and Soft Matter Physics* **90**, 022138 (2014).
 - [41] P. Charbonneau, E. I. Corwin, R. C. Dennis, R. Diáz Hernández Rojas, H. Ikeda, G. Parisi, and F. Ricci-Tersenghi, Finite-size effects in the microscopic critical properties of jammed configurations: A comprehensive study of the effects of different types of disorder, *Physical Review E* **104**, 014102 (2021).
 - [42] P. Rissone, E. I. Corwin, and G. Parisi, Long-range anomalous decay of the correlation in jammed packings, *Physical Review Letters* **127**, 38001 (2021).
 - [43] J. Sohl-Dickstein, The boundary of neural network trainability is fractal, Arxiv Preprint , 2402.06184 (2024).
 - [44] A. Altieri, F. Roy, C. Cammarota, and G. Biroli, Properties of Equilibria and Glassy Phases of the Random Lotka-Volterra Model with Demographic Noise, *Physical Review Letters* **126**, 258301 (2021).
 - [45] C. J. Clopper and E. S. Pearson, The use of confidence or fiducial limits illustrated in the case of the binomial, *Biometrika* **26**, 404 (1934).
 - [46] P. Charbonneau and P. K. Morse, Jamming, relaxation, and memory in a minimally structured glass former, *Physical Review E* **108**, 054102 (2023).
 - [47] N. Xu, J. Bławdziewicz, and C. S. O'Hern, Random close packing revisited: Ways to pack frictionless disks, *Physical Review E - Statistical, Nonlinear, and Soft Matter Physics* **71**, 061306 (2005).
 - [48] D. Frenkel, D. Asenjo, and F. Paillusson, The other entropy, *Molecular Physics* **111**, 3641 (2013).
 - [49] F. Paillusson, Devising a protocol-related statistical mechanics framework for granular materials, *Physical Review E - Statistical, Nonlinear, and Soft Matter Physics* **91**, 012204 (2015).
 - [50] E. Bautista and E. I. Corwin, Basins of Attraction in the Jamming Energy Landscape Have Power-Law Length Distributions, in *Bulletin of the American Physical Society* (Minneapolis, 2023).
 - [51] A. Clauset and C. R. Shalizi, Power-Law Distributions in Empirical Data, *SIAM Review* **51**, 661 (2009).
 - [52] C. P. Massen and J. P. Doye, Power-law distributions for the areas of the basins of attraction on a potential energy landscape, *Physical Review E - Statistical, Nonlinear, and Soft Matter Physics* **75**, 037101 (2007).
 - [53] A. D. Broido and A. Clauset, Scale-free networks are rare, *Nature Communications* **10**, 1017 (2019).
 - [54] G. Folená, P. Charbonneau, P. K. Morse, R. D. H. Rojas, and F. Ricci-Tersenghi, Jamming the Random Lorentz Gas: Configurational Entropy, Crunching Geometry, and Critical Universality, Arxiv Preprint , 2410.05784 (2024).
 - [55] Y. Zhang and S. H. Strogatz, Basins with tentacles, *Physical Review Letters* **127**, 194101 (2021).
 - [56] B. L. Annesi, C. Lauditi, C. Lucibello, E. M. Malatesta, G. Perugini, F. Pittorino, and L. Saglietti, The star-shaped space of solutions of the spherical negative perceptron, *Physical Review Letters* **131**, 227301 (2023).
 - [57] D. Frenkel and A. J. C. Ladd, New Monte Carlo method to compute the free energy of arbitrary solids. Application to the fcc and hcp phases of hard spheres, *J. Chem. Phys* **81**, 3188 (1984).
 - [58] Note that the decay exponents of Fig. 5(e) (see inset) are

much larger than those of panel (d). Thus, interpreting Fig. 5(e) as the success rate of naïve Monte Carlo on a sphere [30], the FIRE basin, while inaccurate, remains much more correlated with the true basin than uniform sampling.

- [59] L. Baker, A. J. Giancola, and F. Allahdadi, Fracture and spall ejecta mass distribution: Lognormal and multifractal distributions, *Journal of Applied Physics* **72**, 2724 (1992).
- [60] T. Ishii and M. Matsushita, Fragmentation of Long Thin Glass Rods, *Journal of the Physical Society of Japan* **61**, 3474 (1992).
- [61] O. Sotolongo-Costa, Y. Moreno-Vega, J. J. Lloveras-González, and J. C. Antoranz, Criticality in Droplet Fragmentation, *Physical Review Letters* **76**, 42 (1996).
- [62] R. Delannay, G. Le Caër, and R. Botet, A simple soluble model of discrete sequential fragmentation, *Journal of Physics A: Mathematical and General* **29**, 6693 (1996).
- [63] K. Falconer, *Fractal geometry: mathematical foundations and applications* (John Wiley & Sons, 2013).
- [64] J. Gostick, Z. Khan, T. Tranter, M. Kok, M. Agnaou, M. Sadeghi, and R. Jervis, PoreSpy: A Python Toolkit for Quantitative Analysis of Porous Media Images, *Journal of Open Source Software* **4**, 1296 (2019).
- [65] D. Vågberg, D. Valdez-Balderas, M. A. Moore, P. Olsson, and S. Teitel, Finite-size scaling at the jamming transition: Corrections to scaling and the correlation-length critical exponent, *Physical Review E - Statistical, Non-linear, and Soft Matter Physics* **83**, 030303(R) (2011).

Box-counting dimension of 2d cuts

To complete the data on distributions of 1d intersection lengths between random lines and basins presented in the main text, we discuss a 2d measure of the fractal dimension of intersections of basins with random 2d planes, such as the slices of Fig. 1 of the main text. To quantify the fractal dimension of basin boundaries, we rely on the Minkowski-Bouligand, or “box-counting” dimension [63], d_B . For non-fractal shapes $d_B = 1$, while fractal shapes have $d_B > 1$. To estimate d_B , we isolate a single basin from a 2d cut such as the ones in Fig. 1 of the main text, then use the `porespy` library [64]. The detailed procedure is described in SI [31].

In Fig. 6(a), we show Gaussian kernel density estimates (KDE) obtained from the histograms of d_B for each method. We show that the mode of the distribution is close to unity ($d_B^{mode} \in [1.05; 1.15]$) when using CVODE or GD, but is shifted to significantly higher values ($d_B^{mode} \in [1.3; 1.4]$) when using FIRE or L-BFGS.

To estimate the effects of finite resolution, in Fig. 6(b), we plot the average box counting dimension $\langle d_B \rangle$ calculated for the n_B largest basins, against n_B (error bars are 95% confidence intervals calculated by bootstrap). We show that as smaller basins are included in the average, the estimated fractal dimension decreases significantly for FIRE and L-BFGS, while it essentially plateaus for ODE solvers. This is due to the finite resolution of slices:

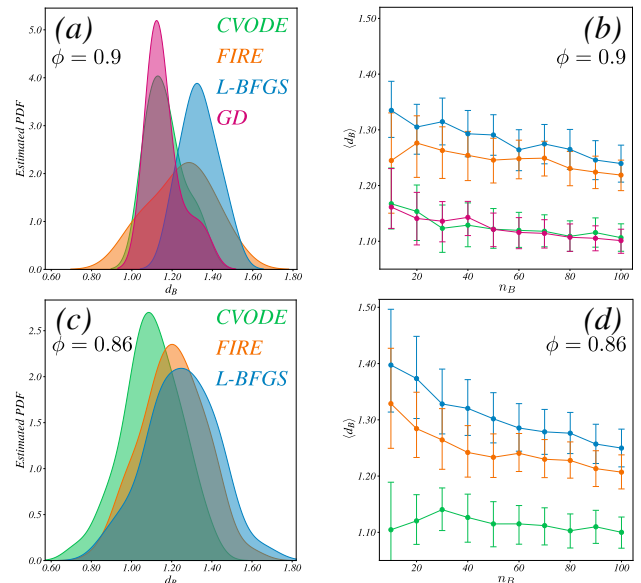


FIG. 6. **Box-counting dimension.** (a) Gaussian kernel density estimate of the PDF of the box counting dimension d_B from top 10 largest basins for $N = 128$ and $\phi = 0.9$, and (b) corresponding average box counting dimension estimated from the top n_B largest basins. In (c), (d), we show the same plots for $N = 128$ and $\phi = 0.86$.

ϕ	d_B (L-BFGS)	d_B (FIRE)	d_B (CVODE)	d_B (GD)
0.9	1.34 ± 0.05	1.24 ± 0.09	1.17 ± 0.05	1.16 ± 0.06
0.86	1.40 ± 0.09	1.33 ± 0.09	1.10 ± 0.08	N/A

TABLE I. **Box-counting dimensions.** Table of d_B values (with bootstrapped 95% confidence intervals) estimated from the 10 largest basins in a slice, for each method.

as we include smaller basins, the scale of the pixel size begins to dominate. As a result, for optimizers, d_B is underestimated when n_B is large. We repeat the same measurement at $\phi = 0.86$, save for GD which becomes prohibitively expensive near jamming. The corresponding plots are shown in Fig. 6(c) and (d) (the slices used for this measurement are shown in SI [31]). The average d_B for $n_B = 10$ are reported in Table I.

Altogether, basins look significantly more fractal ($d_B \gtrsim 1.25$) when identified with optimizers rather than ODE solvers ($d_B \approx 1.1$). As the jamming point is approached, the fractal dimension estimated with CVODE slices does not change significantly, while it becomes larger for L-BFGS and FIRE. Like line measurements, these results suggest that individual basins do not get intrinsically more fractal near jamming—this is just another mirage appearing in optimizer measurements. In particular, the analogy proposed in past work between basins of attraction and Apollonian gaskets [52] quoted a fractal dimension close to 1.3, which is close to what optimizers report but significantly larger than the CVODE values.

Distribution of Energies at Minima

Here we describe the effect of the minimization method on the distribution of energies at minima, mentioned in the main text. For each method, and for $N \in \{8, 32, 128, 512, 2048\}$, we use the same 10^6 initial conditions for optimization, uniformly drawn at random in configuration space, at $\phi = 0.9$. We then collect the energies at the minima, and study their distributions. In Fig. 7(a), we plot the differences between the mean total energies obtained with FIRE/L-BFGS and CVODE, as a function of N . We report a growing bias towards lower energies in both FIRE and L-BFGS as N grows, meaning that the choice of method does affect the distribution of energies. It is worth noting that FIRE and L-BFGS do not create any new minima compared to CVODE, so that this difference is solely due to how often a given minimum is found—or, in other words, to the distribution of basin volumes being altered. To investigate the effect of this phenomenon further, we plot the relative errors on mean energy per particle against $1/N$ in Fig. 7(b). We show that the relative error in fact decays with N , meaning that the bias of Fig. 7(a) is subextensive. However, as indicated by a dashed line, the error vanishes algebraically slowly and with a small power, roughly as $N^{-1/6}$ for both FIRE and L-BFGS. While with our choice of potential the numerical value of the error remains rather small because the prefactor of the algebraic decay is small, another potential could display equally slow convergence with N but with larger prefactors. Finally, we assess the effects of the minimization method on the full distributions of energies. In Fig. 7(c), we plot the empirical distributions obtained for total energies at minima for $N = 2048$ particles. The distributions obtained through FIRE and L-BFGS display a systematic bias towards lower energies throughout. However, as shown in Fig. 7(d), the *shape* of the distribution is only very weakly modified, as empirical distributions of the reduced energies at minima $e \equiv (E - \langle E \rangle)/\sigma_E$, with σ_E the empirical standard deviation, overlap almost perfectly.

Jamming point

We study the effect of optimizers on the location of the jamming point. We randomly sample uniform initial conditions in configuration space per packing fraction across a range of ϕ , and report the fraction P_J of them that falls into a minimum with all methods. The results are shown in Fig. 8(a) for $N = 16$ and 10^5 ran-

dom points. We show that there is a noticeable shift in the curve when switching to optimizers. We perform this measurement across N , using 10^3 points per N and density (see SM [31] for full curves) and measure the packing fraction ϕ_J with $P_J = 1/2$. The result is shown in Fig. 8(b). Curves roughly follow power laws of the form

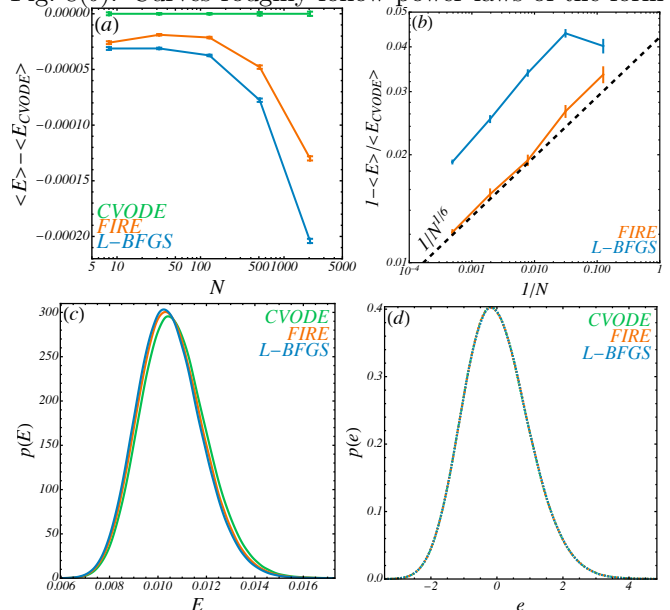


FIG. 7. **Energies at minima.** (a) Differences between mean energies of minima for each method and the mean energies obtained with CVODE against N , in log-linear scales. The CVODE line is represented to indicate standard error on the CVODE mean. (b) Relative error on the energies with respect to CVODE against $1/N$, in log-log scales. The dashed black line indicates $1/N^{1/6}$. (c) Empirical distribution of energies E at minima for all three methods for $N = 2048$. (d) Corresponding empirical distribution of reduced energies $e \equiv (E - \langle E \rangle)/\sigma_E$, in dashed lines. Throughout the figure, we encode CVODE by green, FIRE by orange, and L-BFGS by blue. Error bars on the mean are obtained by bootstrapping over 1000 subsamples.

$\phi_J(\infty) - \phi_J(N) \propto 1/N^\theta$ with $\phi_J \approx 0.842$ and $\theta \approx 0.67$ as previously reported [35, 65]. Like for energies, a deviation between optimizers and CVODE remains noticeable at large N . In the inset, we show the evolution of the relative difference of ϕ_J between optimizers and CVODE, showing a trend slower than $N^{-1/3}$. In short, optimizers introduce a bias on sampled minima that biases finite-size estimates of the jamming density, with a slowly decaying error.

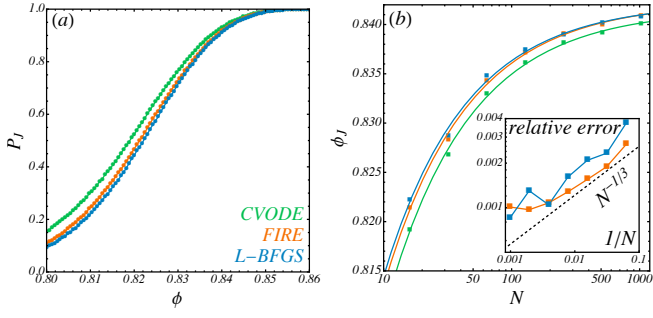


FIG. 8. **Jamming Point** (a) P_J against ϕ for $N = 16$ across methods. Student-T 95% confidence intervals are smaller than symbols. (b) ϕ_J against nyuchemistry N across methods. Solid lines are critical power-law fits. Inset: relative error on ϕ_J compared to CVODE against N . Dashed black line: $N^{1/3}$ scaling (guide for the eyes).

Supplementary Information for “The Basins of Attraction of Soft Sphere Packings Are Not Fractal”

Praharsh Suryadevara,¹ Mathias Casiulis,^{1,2} and Stefano Martiniani^{1,2,3,4}

¹*Center for Soft Matter Research, Department of Physics, New York University, New York 10003, USA*

²*Simons Center for Computational Physical Chemistry, Department of Chemistry, New York University, New York 10003, USA*

³*Courant Institute of Mathematical Sciences, New York University, New York 10003, USA*

⁴*Center for Neural Science, New York University, New York 10003, USA*

(Dated: July 8, 2025)

I. MINIMIZATION AND BASIN IDENTIFICATION STRATEGIES

In the main text, we present comparisons between different numerical strategies to map out the basins of attractions of minima in the potential energy landscape of soft repulsive spheres. Here, we first describe the minimization algorithms we used in more detail and justify our choice of ODE solver. Then, we discuss how we determine that a minimization has converged, and how we match minima found from different minimizations. Finally, we provide full tables of parameters for optimizers and ODE solvers used in this work.

A. Basin Mapping strategies

The basins of attraction of the potential energy landscape are defined through steepest descent dynamics. If $\mathbf{X} = (x_1, y_1, \dots, x_N, y_N)$ represents a position in the $(N - 1)d$ dimensional space over which the energy landscape $E(\mathbf{X}; \mathbf{R})$ is defined, and $\mathbf{R} = (R_1, R_2, \dots, R_N)$ is the vector of all particle radii (here assumed fixed), the steepest descent dynamics are given by the ordinary differential equation (ODE)

$$\dot{\mathbf{X}}(t) = -\nabla_{\mathbf{X}} E(\mathbf{X}(t); \mathbf{R}), \quad (\text{S1})$$

with the initial condition $\mathbf{X}(t = 0) = \mathbf{X}_0$ specifying which point to start from. A basin is then uniquely identified by the infinite-time limit value of the solution to these dynamics, $\mathbf{X}_\infty = \lim_{t \rightarrow \infty} \mathbf{X}(t)$. While there are other fixed points in the landscape (saddles, maxima), they are unstable, so that their “basin” is reduced to a point, and sampling random initial points \mathbf{X}_0 in configuration space almost surely leads to a minimum in the infinite time limit. Thus, the basin identification problem reduces to that of computing the map $\mathbf{X}_0 \mapsto \mathbf{X}_\infty$, that transforms the configuration space of repulsive spheres into a finite set of attractors.

The ODEs of Eq. S1 may be solved numerically by introducing discrete time steps. The most naïve approach to integrate it is the forward Euler scheme, which has been the dominant approach to identify basins. The Forward Euler approach relies on the discretization,

$$\mathbf{X}(t + dt) \approx \mathbf{X}(t) - dt \nabla_{\mathbf{X}} E(\mathbf{X}(t); \mathbf{R}), \quad (\text{S2})$$

which is unstable on stiff problems such as the one we consider, leading to large errors, unless dt is made very small [1]. This algorithm is often simply referred to as “gradient descent”, or even “steepest descent”, in the jamming and glass communities. In order to increase the accuracy of the method, it is beneficial to introduce adaptive time-stepping. That is why, in the main text, our “GD” method (see Fig. 2 of the main text) relies on the adaptive time-stepping proposed in the context of soft-sphere packings in Ref. 2, where dt is controlled by a parameter ϵ based on the cosine similarity between successive gradients,

$$\hat{\mathbf{g}}(t) \cdot \hat{\mathbf{g}}(t + dt) > 1 - \epsilon, \quad (\text{S3})$$

where $\hat{\mathbf{g}}(t) = \nabla_{\mathbf{X}} E(\mathbf{X}(t); \mathbf{R}) / |\nabla_{\mathbf{X}} E(\mathbf{X}(t); \mathbf{R})|$. In practice, at each step, a new location is proposed according to Eq. S2 and, if criterion S3 is met, the step is accepted. Otherwise it is rejected, dt is decreased, and another candidate location is proposed. Additionally, if the cosine similarity condition is satisfied for n successive steps, then the stepsize is multiplied by n . Recent work suggests [2] that this adaptive forward Euler algorithm has a better time-accuracy trade-off than other described gradient descent variations in the literature [3, 4]. Yet, the inherent instability of the forward-Euler scheme means that the lowest dt required for this algorithm to converge to the true mapping between initial points and minima is very small, and as such it has a prohibitive computational cost in most cases.

As a result, many past works have opted for algorithms that do not solve the dynamics S1, but instead rely on proxy dynamics. In the context of soft sphere packings, careful studies have shown good accuracy for basin mapping in

spite of the proxy dynamics, *e.g.* Ref. 3. However, these studies were restricted to very small systems ($d(N-1) < 5$) and, as we show in this work, the accuracy of these methods plummets as N grows. Below, we describe the two main methods used in the literature.

On the one hand, some works, *e.g.* Refs. [5, 6] have opted for quasi-Newton methods such as L-BFGS [7], that use information about the second derivative of the energy to accelerate convergence to the minimum. In a nutshell, these methods rely on a second-order Taylor expansion of the energy around any point \mathbf{X}_0 ,

$$E(\mathbf{X}_0 + \delta\mathbf{X}, \mathbf{R}) \approx E(\mathbf{X}_0; \mathbf{R}) + \nabla_{\mathbf{X}} E(\mathbf{X}_0; \mathbf{R}) \cdot \delta\mathbf{X} + \frac{1}{2} \delta\mathbf{X}^T \cdot \overline{\overline{\mathbf{H}}}(\mathbf{X}_0; \mathbf{R}) \cdot \delta\mathbf{X}, \quad (\text{S4})$$

where $\overline{\overline{\mathbf{H}}}$ is the Hessian matrix of the energy, and $\delta\mathbf{X}$ is a small displacement vector in configuration space, such that $\|\delta\mathbf{X}\|^2$ is small compared to the scales of variation of the gradient and Hessian. One may then compute the derivative of this expression with respect to $\delta\mathbf{X}$ to find an optimal update,

$$\nabla_{\mathbf{X}} E(\mathbf{X}_0 + \delta\mathbf{X}; \mathbf{R}) \approx \nabla_{\mathbf{X}} E(\mathbf{X}_0; \mathbf{R}) + \overline{\overline{\mathbf{H}}}(\mathbf{X}_0; \mathbf{R}) \cdot \delta\mathbf{X}. \quad (\text{S5})$$

The optimal update corresponds to the case $\nabla_{\mathbf{X}} E(\mathbf{X}_0 + \delta\mathbf{X}; \mathbf{R}) = 0$, that would converge to the minimum in a single step in a quadratic energy landscape. To achieve this, the ‘‘Newton’’ step is then given by

$$\delta\mathbf{X}_N = -\overline{\overline{\mathbf{H}}}^{-1}(\mathbf{X}_0; \mathbf{R}) \cdot \nabla_{\mathbf{X}} E(\mathbf{X}_0; \mathbf{R}). \quad (\text{S6})$$

A quasi-Newton method is one that replaces the inverse of the Hessian, which is costly to compute, by a cheaper numerical evaluation. The issue with such methods is that they are guaranteed to map a point to the steepest descent minimum only if the energy landscape is strictly convex. As a result, this method is in general likely to introduce *some* error in the mapping between initial points and minima defined through steepest descent.

Many other works have relied on momentum-based methods, *e.g.* Refs. [8–12], most notably FIRE [13] where a small amount of inertia is added to the dynamics. Instead of the gradient descent equation, Eq. S1, FIRE solves the second-order ODE [13]

$$m\ddot{\mathbf{X}}(t) + \gamma(t) \left(\dot{\mathbf{X}}(t) + |\dot{\mathbf{X}}(t)| \frac{\nabla_{\mathbf{X}} E(\mathbf{X}(t); \mathbf{R})}{|\nabla_{\mathbf{X}} E(\mathbf{X}(t); \mathbf{R})|} \right) = -\nabla_{\mathbf{X}} E(\mathbf{X}(t); \mathbf{R}), \quad (\text{S7})$$

with m a mass and $\gamma(t)$ a damping coefficient. The effect of the term proportional to γ is to re-orient the velocity onto the steepest descent direction, but with a delay. In FIRE, $\gamma(t)$ is dynamically updated so as to avoid uphill motion [13]. Although the addition of momentum accelerates convergence to a minimum, the dynamics are very different from those of steepest descent. We use a strictly downhill variant of FIRE with limited stepsize [14].

B. Choice of ODE solver

We investigate which ODE solver offers the best possible time-for-error trade-off. Due to the stiffness of the problem, we focus on adaptive implicit solvers. We test a number of candidate algorithms on the energy landscape of Hertzian disk packings, and report a benchmark in Fig. S1. The benchmark consists of work-precision diagrams computed for $N = 8, 16, 32, 64, 128$, with the same size distribution as in the main text. For each system size, we spawn 100 random starting points \mathbf{X}_0 , drawn uniformly in the periodic square box $[0; L]^2$, then solve the steepest descent dynamics, Eq. S1, using a wide range of ODE solvers available in the Julia *DifferentialEquations.jl* package[15], including *lsoda*, a Fortran ODE solver library that switches between implicit and explicit methods based on a stiffness criterion. For $N = 32, 64$, and 128, we restrict ourselves to more performant methods to avoid prohibitive computation times. The error in adaptive ODE solvers is managed via a relative local error tolerance, `rtol`, and an absolute error tolerance `atol`, that ensure at each step that the trajectory does not stray away from the true ODE solution more than a specified amount (using a relative and an absolute distance, respectively). The absolute error tolerance `atol` sets the error bound when the coordinates are close to the origin, where the relative indicator `rtol` is ill-defined. Here, each ODE solver is run independently for a variety of values of the relative tolerance parameter `rtol`, and for a large enough integration time that the distance of the final point to the minimum is less than 10^{-2} , in this case $t_{\text{stop}} = 10000$. We ensure that the relative performance of ODE solvers is insensitive to the stopping time. We then measure for each computed trajectory: 1) the time the computation took (in seconds), and 2) the maximal distance a particle deviates from the true steepest descent path over the whole trajectory,

$$d_{\text{max}}^{\text{solver}}(\mathbf{X}_0, \text{rtol}) \equiv \max_{0 \leq t \leq t_{\text{stop}}} \|\mathbf{X}_{\text{solver}}(t; \mathbf{X}_0, \text{rtol}) - \mathbf{X}_{\text{ref}}(t; \mathbf{X}_0)\|, \quad (\text{S8})$$

where $\mathbf{X}_{\text{solver}}(t; \mathbf{X}_0, \text{rtol})$ is the trajectory found by the solver from the initial position \mathbf{X}_0 and at a given value of rtol , and \mathbf{X}_{ref} is the steepest descent trajectory. We then construct a Mean Trajectory Distance, defined as the average over random initializations \mathbf{X}_0 of $d_{\text{max}}^{\text{solver}}$. In practice, we estimate the Mean Trajectory Distance using 100 evenly spaced points along the trajectory. The reference trajectory \mathbf{X}_{ref} is obtained using *CVODE_BDF* with stringent tolerances ($\text{rtol} = \text{atol} = 10^{-12}$).

The results show that among the wide range of parameters we use, *CVODE_BDF* [16, 17] (an adaptive-step implicit method that is part of the SUNDIALS suite) outperforms other ODE solvers, with *QNDF* and *FBDF* also showing competitive performance as system size increases. We emphasize that all ODE solvers converge to the same trajectory as rtol is decreased, and our calculations are always performed in the regime where our identified basin is independent of precise solver parameters. We therefore adopt *CVODE* as our reference ODE solver in the rest of the paper.

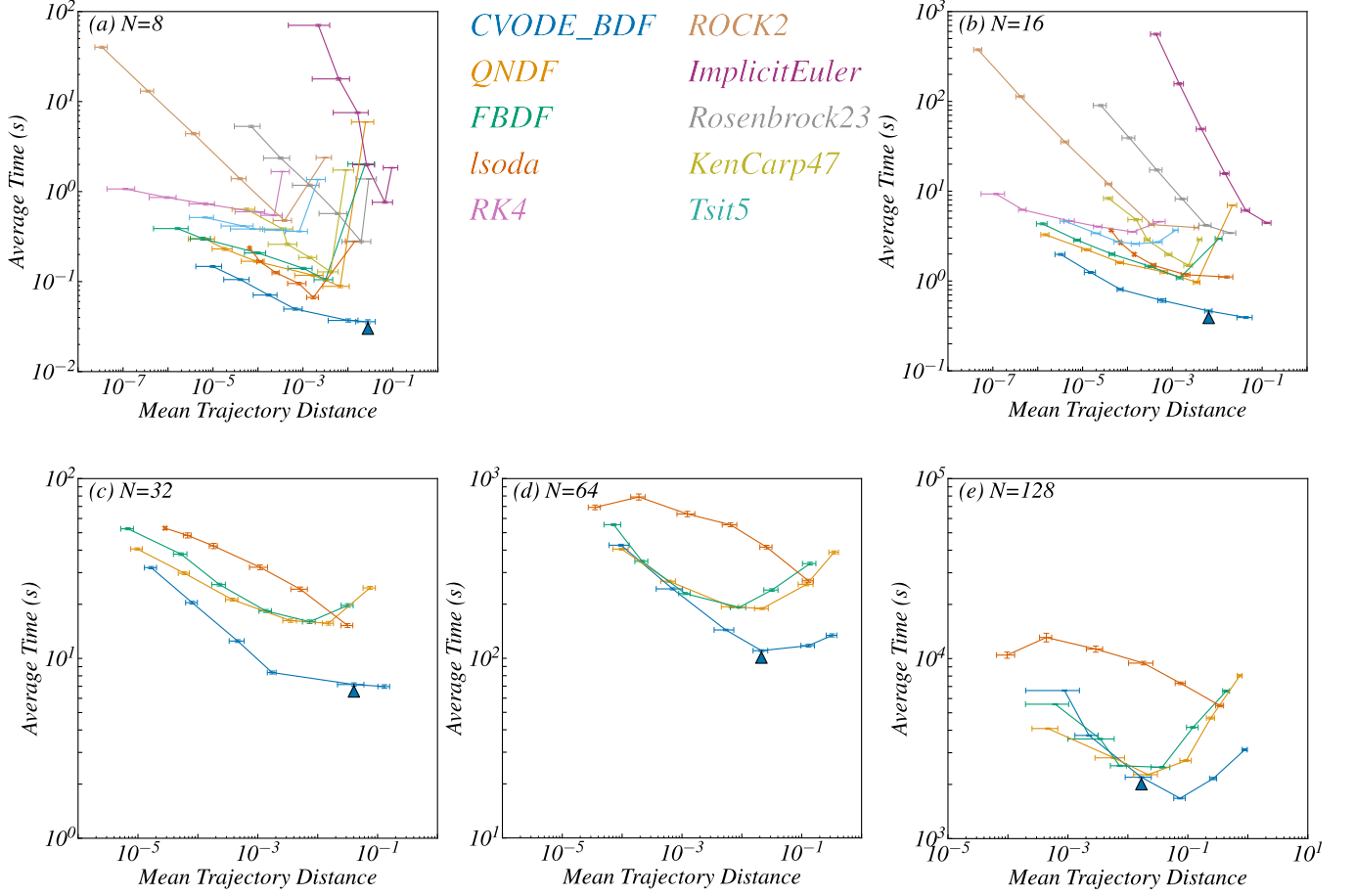


FIG. S1: **Benchmarking ODE solvers.** (a)–(e) Plots of the Mean Trajectory Distance versus Average Computation Time for different numbers of particles $N = 8, 16, 32, 64$, and 128 , respectively. Error bars represent the standard error of the mean (SEM) for both the Mean Trajectory Distance and Average Computation Time. Points highlighted by filled triangles correspond to the maximum tolerance values used among all calculations.

C. Performance on other systems

To rule out the possibility that *CVODE* is optimal only for our choice of interaction potential, we perform the same benchmark as in Sec IB on 3 other systems, spawning 100 random starting points uniformly in configuration space for each of them.

In Fig. S2(a), we consider a set of $N = 8$ soft spheres interacting via a harmonic potential,

$$V_{ij}(r_{ij}) = \varepsilon \left(1 - \frac{r_{ij}}{R_i + R_j} \right)^2 \mathbb{1}(r \leq R_i + R_j), \quad (\text{S9})$$

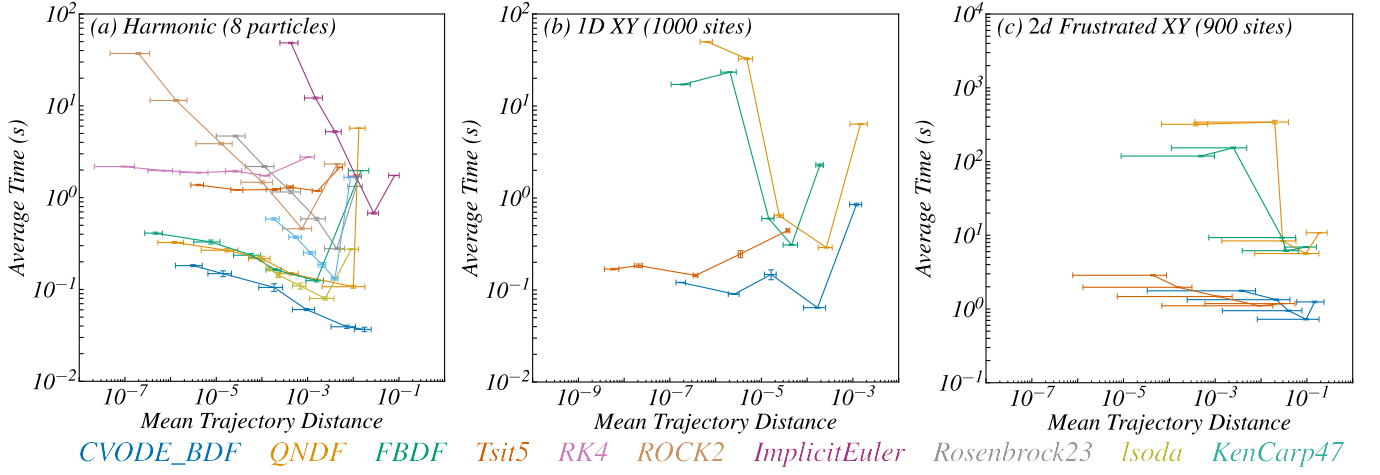


FIG. S2: **Benchmarking ODE solvers on other systems.** (a) Interacting pairwise potential with harmonic interactions (b) 1D XY model (Kuramoto) (c) Frustrated XY model on a triangular lattice. Error bars represent the standard error of the mean (SEM) for both the Mean Trajectory Distance and Average Computation Time. For the XY model [(b) and (c)] we utilize Jacobian Free GMRES solvers provided by the libraries for all implicit methods (CVODE, QNDF, FBDF) for speed.

rather than a Hertzian one. We show that CVODE outperforms other solvers in a way similar to that described in the case of a Hertzian potential, Fig. S1.

In Figs. S2(b) – (c), we consider variations on the XY model [18], with the energy function

$$E = - \sum_{i=1}^N \sum_{j \in \partial i} J_{ij} \hat{\mathbf{s}}_i \cdot \hat{\mathbf{s}}_j, \quad (\text{S10})$$

where $\hat{\mathbf{s}}_i = (\cos \theta_i, \sin \theta_i)$ is a two-dimensional unit vector parametrized by an angle $\theta_i \in [0; 2\pi)$, J_{ij} is the interaction constant between spins i and j ($J_{ij} > 0$ is aligning, $J_{ij} < 0$ is anti-aligning), and ∂i is the neighborhood of spin i , which depends on the chosen geometry for the problem. Note that the dynamical system defined by the steepest descent equation for Eq. S10 with aligning interactions is also known as the Kuramoto model, whose basins of attraction have been previously investigated [19–22]. In Fig. S2(b), we choose a 1d geometry with nearest-neighbor interactions only, and we set $J_{ij} = +1$ between neighbors, defining a usual ferromagnetic XY model. In Fig. S2(c), we choose a 2d triangular lattice with $J_{ij} = -1$ interactions between nearest neighbors, thus defining a fully-frustrated XY model [23–25], a classical model of deterministic spin glass. In both cases, Tsit5 [15, 26], a variant of RK4, performs comparably to CVODE. This implies that the steepest descent equation in the case of the XY model, even in a glassy regime, is not stiff enough that there is a significant performance gap between implicit and explicit methods. Note that we checked that *lsoda*, the solver used in Refs. [21, 22], performs significantly worse than the solvers we show in this benchmark, so that we do not show it in Fig. S2.

D. Convergence Criterion

Throughout this study, a convergence criterion is needed to decide whether an optimizer has run for sufficiently long that it has approached its infinite-time attractor. Far from jamming (here, empirically, for packing fractions $\phi \gtrsim 0.86$), the Hessian eigenvalues are relatively large throughout the landscape, so that we use a simple gradient-based convergence criterion: we end ODE solving and optimizations when $\|\mathbf{g}\| < 10^{-10}$. However, as the system gets closer to jamming, the Hessian eigenvalues may become small, as the energy landscape flattens. As a result, it is possible to have very small forces on particles far from the minimum, so that a purely gradient-based criterion can trigger premature termination of the minimization. To circumvent this issue, we employ a Newton-step-based convergence criterion that uses a second-order estimate of the distance to the minimum,

$$\delta \mathbf{X}_{\min} \approx \left(\overline{\mathbf{H}}(\mathbf{X}) + \lambda(\mathbf{X}) \overline{\mathbf{I}} \right)^{-1} \mathbf{g}(\mathbf{X}), \quad (\text{S11})$$

where \mathbf{g} is the gradient, $\overline{\mathbf{H}}$ is the Hessian, $\overline{\mathbf{I}}$ is the identity matrix, and λ is chosen to ensure that $H + \lambda I$ remains well-conditioned. In practice, $\lambda = \max(2|\lambda_{\min}|, \gamma \lambda_{\text{avg}})$, where λ_{\min} and λ_{avg} are the minimum and average Hessian eigenvalues at \mathbf{X} , respectively, and $\gamma = 0.1$. We consider the dynamics converged when

$$\|\delta \mathbf{X}_{\min}\| < 10^{-5}. \quad (\text{S12})$$

This threshold is three orders of magnitude smaller than the maximal distance between non rattler particles used to declare two minima as different, 10^{-2} . The reason for using a smaller value is that Newton steps are only a heuristic and may lower accuracy if one does not make its range smaller than every other scale of the landscape near minima. We check that this value does not introduce errors compared to a very small gradient criterion in the landscape of Hertzian disks, but comes at a lower computational cost.

E. Minima matching procedure

It is crucial to be able to accurately determine whether 2 points obtained as large-time limits of numerical dynamics map to one and the same minimum of the energy landscape. In the context of jammed packings, the procedure is complicated by the presence of rattlers, *i.e.* particles that can move over a finite-measure set of positions without changing the overall energy of the system. Thus, to match minima, we first identify all rattlers in the system by checking whether they are contained by a convex hull of non-rattler neighbors. We then check whether the remaining particles and the number of contacts are enough to create a stable backbone, using the fact that we need at least $2(N_{\text{stable particles}} - 1) + 1$ contacts for a stable backbone. If there are not enough contacts, we conclude that the configuration is a fluid state, and is simply tagged as fluid. Otherwise, we conclude that the minimum is jammed.

To identify whether two jammed minima are different, we first check whether they have the same number of rattlers—if not, they are different. If they do, to account for translational symmetry, we superimpose the first non-rattler particle of each packing onto each other (recall that the set of radii is the same so that there is a clear particle identity). The two minima are identified as different if the maximal distance across all non-rattler particles with the same radius is greater than $\text{dtol} = 10^{-2}$. In practice, at jamming densities over 0.85, and across various minima, all matches we find correspond to maximal distances smaller than 10^{-4} when we set a gradient tolerance $\text{tol} = 10^{-10}$ in the convergence criterion (see Sec. IF). Our choice of dtol is the largest value that doesn't lead to appreciable change in the landscape at any value of (N, ϕ) .

F. Choices of solver parameters

In this section, we provide complete lists of parameter for all solvers used in the main text—namely, CVODE, FIRE, L-BFGS, and Gradient Descent. Whenever relevant, we also provide a rationale for these choices.

1. CVODE Parameters

Many adaptive ODE solvers, including CVODE, adjust their step size by imposing an upper bound on the estimated local error for each step. As noted in Sec. I, this bound is specified by two tolerance settings: relative error (rtol) and absolute error (atol). However, constraining this local error estimate does not guarantee that the global error will adhere to the same bounds, particularly in systems where small errors can lead to diverging trajectories. To address this limitation, we set values for tolerances based on an analysis of the accuracy of the mapping $\mathbf{X}_0 \mapsto \mathbf{X}_\infty$ between random initial points and their corresponding final minima.

To assess this accuracy, one needs a reference (a ground truth). Relying on the fact that CVODE is an ODE solver, and thus asymptotically converges to the true steepest-descent trajectories at vanishing rtol , we expect minimal error when rtol is small enough that the mapping remains unchanged over large random sets of points as we decrease rtol . Across all our simulation parameters, this is achieved when rtol is set to 10^{-14} .

Using this reference, we assess performance at larger tolerances by running CVODE from approximately 10000 random initial points at each rtol value. We define an accuracy for each rtol as the fraction of initial points that converge to the same minimum as when $\text{rtol} = 10^{-14}$. Results are shown in Fig. S3, where we plot accuracies and computation times against rtol at all system sizes for which CVODE is considered in the paper. We also report performance based on whether we switch on an iterative Newton-Krylov scheme [27] provided within CVODE [16, 17] to solve an implicit time-stepping equation instead of using the dense Hessian. For each N , we highlight the rtol and choice of scheme (iterative or dense) corresponding to the fastest time with $> 98\%$ accuracy at identifying basins accurately. This rtol is the value we use in practice.

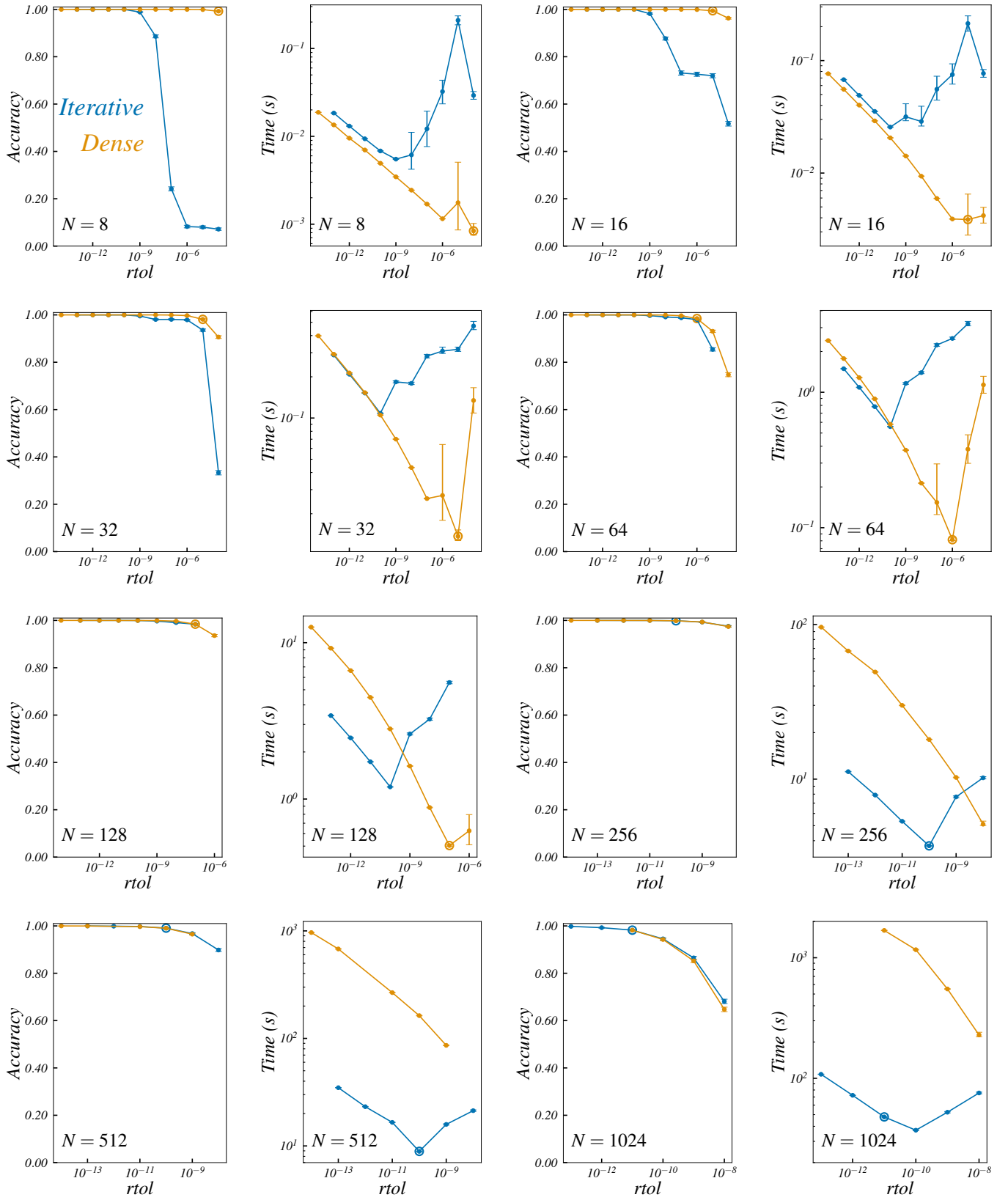


FIG. S3: **CVODE Accuracy and Time vs Tolerance.** For each N , we vary $rtol$ and report accuracy and time, averaged across 10^4 random initial conditions. Error bars represent Clopper-Pearson confidence intervals for accuracy and standard error for time. Highlighted points correspond to points used in the main text, corresponding to $> 98\%$ accuracy. The point at the lowest $rtol$ is taken to have accuracy 1.0

We summarize our choices of `rtol` and scheme for each N in Table S1, where we also give values for accuracies larger than 95%. Note that the optimal time to attain these accuracies involves switching on the iterative scheme at sizes $N > 64$, which leads to a slight change of trend of time scalings at the junction $N = 64$.

System Size	<code>rtol</code> (acc $\gtrsim 95$)	<code>rtol</code> (acc > 98)	Iterative
8	10^{-4}	10^{-7}	False
16	10^{-5}	10^{-7}	False
32	10^{-5}	10^{-7}	False
64	10^{-6}	10^{-7}	False
128	10^{-7}	10^{-8}	True
256	10^{-8}	10^{-9}	True
512	10^{-9}	10^{-10}	True
1024	10^{-10}	10^{-11}	True

TABLE S1: **Tolerances for CVOICE.** Table of CVOICE tolerances we choose. For small systems, while a higher `rtol` is optimal for performance, the resulting numerical noise can prevent the gradient from satisfying the 10^{-10} convergence threshold close to a minimum. Here iterative means that an iterative Newton-Krylov scheme is used to solve the Newton's equation instead of using the dense Hessian.

Note that while the matrix structure for the Hessian is sparse, we are not aware of already available methods that may take advantage of this property, because the sparsity structure constantly changes as particles start or stop interacting through the minimization process.

2. FIRE, LBFGS, and Gradient Descent parameters

We employ the FIRE and L-BFGS algorithms as implemented in the `pele` package [28], which adhere to the recommendations by Ref. 3 to generate accurate basins. To prevent excessively large step sizes, we cap the maximum step at

$$\Delta_{\max} = \frac{\mu_s}{10} \quad (\text{S13})$$

with μ_s the mean radius of the smaller particles in our bidisperse distribution of radii. In the basin volume calculations, however, we use a different bound to be consistent with parameter choices in Ref. 10,

$$\Delta_{\max}^{\text{BV}} = \frac{R_{\min}}{4} \quad (\text{S14})$$

with R_{\min} the smallest radius. In practice, for our choice of distributions, we typically have $\Delta_{\max}^{\text{BV}} \approx 2\Delta_{\max}$.

In our FIRE implementation, we incorporate an additional safeguard: the minimizer is prevented from taking uphill steps by halting and resetting momentum, as in Ref. 10. The list of FIRE parameters for the `pele` implementation used in the paper are given in Tab. S2. `finc` determines the factor to be applied to dt after `Nmin` steps, $dt' = \text{finc } dt$, if the velocity is downhill (i.e pointing in the direction of the gradient). If we encounter an uphill step, then we reduce dt by multiplying it by `fdec`, $dt' = \text{fdec } dt$. The maximum timestep, `dtmax`, is set to 1.

Our L-BFGS parameters are listed in Tab. S3. Here, `M` controls how well the algorithm approximates the Hessian, `maxErise` determines how much the energy can rise due to the method, (in this case 0), `H0` determines the initial approximate inverse Hessian. We use the default parameter `M = 1` as recommended by Ref. [3].

Finally, in the variant of Gradient Descent adapted from Ref. 2 and described in Sec. IA, we use the parameters given in Tab. S4. Here ϵ is a bound on the cosine similarity between successive gradients. dt_{initial} is the starting value of the timestep dt . If $n_{\text{backtrack}}$ successive steps satisfy the cosine similarity condition then we modify the timestep $dt = n_{\text{backtrack}} dt$, and if the condition is violated, we reduce the timestep by doing $dt = dt/n_{\text{backtrack}}$.

II. DETAILED NUMERICAL EXPERIMENTS

In this section, we describe numerical methods used to produce the data discussed in the main text in complete detail.

Parameter	Value
dtstart	0.1
dtmax	1
maxstep	0.5
Nmin	5
finc	1.1
fdec	0.5
fa	0.99
astart	0.1
stepback	True
tol	10^{-10}

TABLE S2: FIRE algorithm parameters

Parameter	Value
tol	10^{-10}
M	1
maxstep	0.1
maxErise	10^{-10}
H0	0.1

TABLE S3: L-BFGS algorithm parameters

A. Low-dimensional intersections: $2d$ slices and $1d$ line cuts

To produce $2d$ slices of the energy landscape color-coded by basin, such as Fig. 1 of the main text, we first sample a single configuration \mathbf{X}_0 uniformly in $[0; L]^{Nd}$. We then randomly sample two orthogonal directions, encoded by two unit vectors $\hat{\mathbf{n}}_1$ and $\hat{\mathbf{n}}_2$ such that $\hat{\mathbf{n}}_1 \cdot \hat{\mathbf{n}}_2 = 0$ and construct a grid of configurations centered around that random point, *i.e.* a set of points with locations $\mathbf{X}_{pq} = \mathbf{X}_0 + pP_x\hat{\mathbf{n}}_1 + qP_y\hat{\mathbf{n}}_2$ with $(p, q) \in \mathbb{Z}^2$ such that p spans N_1 integers and q spans N_2 integers (both with ranges centered on 0), and $P_x, P_y > 0$ are the spacings between two measurement points along the two axes. The output is translated into a $N_1 \times N_2$ picture, where each pixel is colored by the basin it belongs to. The list of colors is generated using the Glasbey colormap [29] to ensure that the color corresponding to each minimum is perceptually distinct.

In Fig 1 of the main text, we produce pictures of 1920×1080 pixels that correspond to a rectangle in configuration space with side-lengths $12\mu_s \times 6.75\mu_s$ (in units of the mean radius μ_s of the small disks). For Fig. 2 of the main text, and all $N = 128$ cuts in this document, we produce 800×800 pictures corresponding to squares in configuration space with side-lengths $0.44\mu_s \times 0.44\mu_s$. This configuration-space width is chosen so that the $2d$ density of basins on the slices would be fairly similar to that of Fig. 1 of the main text. In this document, we also produce slices for $N = 8$ (see Fig. S8). They are produced using 800×800 pictures corresponding to squares in configuration space with side-lengths $10\mu_s \times 10\mu_s$.

Line intersections are produced in a similar way. We start by selecting a configuration uniformly, then sample a random direction uniformly, thus defining a line. On that line, we define a segment symmetrically around the starting configuration, with a total length $L_S \approx 10\mu_s$ for $N = 16$, similar to the sidelengths of one of the $2d$ slices of Fig. 1. We then divide that segment into 10^6 regularly spaced points, which we use as initial conditions for optimization, and we tag the basins they fall into. Having thus constructed a discretized map of basins on the line, we list all pairs of neighboring pixels falling into distinct basins. At each such pair, we define a new collection of points on the line, with a resolution 10^2 finer, and linking the 2 neighboring pixels. We run optimizations at these new points

Parameter	Value
ϵ	10^{-2}
dt_{initial}	10^{-5}
$n_{\text{backtrack}}$	5

TABLE S4: Gradient Descent algorithm parameters

to better resolve the junction between the two basins, possibly uncovering new basins. Finally, we reconstruct the intersection lengths between the basins and the line using the two resolutions. Note that, in principle, the zoom being performed selectively at junctions found at the base resolution could introduce biases in the measured lengths. However, we here use resolutions much finer than in the $2d$ cuts from the main text, as the base resolution before zooming is about 1000 times finer than that of Fig. 1 of the main text (the zoomed in version is thus 10^5 times finer than Fig. 1). We also check that we never see new basins within the bulk of a basin when switching to finer scales. In other words, empirically, basins are regular enough that we do not expect a measurable effect of zooming everywhere versus zooming only at intersections. Furthermore, note that for the data shown in Fig. 3 of the main text, the peak in the distribution of log-lengths obtained with CVODE is already visible before the zoom, so that the zoom helps resolve single-pixel intersections but does not artificially introduce a peak into the distribution.

B. Video caption

The video attached to the article is obtained as a succession of $2d$ slices of the energy landscape similar to the ones shown in Figs. 1 and 2 of the main text, for a system of $N = 16$ Hertzian disks at $\phi = 0.9$. To obtain motion along a closed trajectory, and thus a looping video, we first define a random $2d$ slice in the usual way, see Sec. II A. That slice is defined by a random point \mathbf{X} in configuration space, and two orthogonal unit vectors $\hat{\mathbf{n}}_1$ and $\hat{\mathbf{n}}_2$. We then sample a third and fourth random direction $\hat{\mathbf{e}}_3$ and $\hat{\mathbf{e}}_4$, and use them to construct the unit vectors $\hat{\mathbf{n}}_3$ and $\hat{\mathbf{n}}_4$ such that $\hat{\mathbf{n}}_i \cdot \hat{\mathbf{n}}_j = \delta_{ij}$ for $(i, j) \in \{1, 2, 3, 4\}^2$. Using the two vectors perpendicular to the starting slice, we define a circular trajectory in configuration space and generate regularly spaced slices along it, such that the successive slices are always perpendicular to the circle and are spaced by a distance equal to the size of a pixel. We then match minima across all slices so that any one basin is encoded by the same color across slices. The resulting collection of slices forms a continuous-looking video that hints at a smooth $3d$ structure of basins.

C. Fractal analysis of slices

In this section, we describe in detail the procedure used to measure bounding-box dimensions of $2d$ slices of basins. The box-counting dimension is defined as

$$d_B = \frac{\log(N(\ell_B))}{\log(\ell_B)}. \quad (\text{S15})$$

where $N(\ell_B)$ is the number of cubic boxes with sidelength ℓ_B that are needed to cover a shape.

Starting from a $2d$ slice of configuration space such as Fig. 1 of the main text, we crop the image to the smallest bounding box that encloses the basin boundary, with a padding of $L/16$ to mitigate boundary effects, then convert the picture into a binary map with values 1 in the basin, 0 elsewhere. We then feed the result into the `porespy` package [30] to count $N(\ell_B)$. To estimate d_B , we perform a linear fit on the $\log(N(\ell_B))$ versus $\log(\ell_B)$ data, excluding the largest scales so as to mitigate finite-size effects due to the finite slice size. We thus measure a fractal dimension for the selected basin: a smooth (non-fractal) basin would have dimension $d_B = 1$, a fractal one $d_B > 1$. To characterize the landscape, in practice, we repeat this measurement for the largest (in number of pixels) n_B basins in a slice. This choice is similar to the one in Ref. [31], where the authors also show in the example of the Random Lorentz Gas that the largest basins are the most likely to be fractal.

The slices used for $\phi = 0.9$ are those of Fig. 2 of the main text, while the ones used for $\phi = 0.86$ are shown in Fig. S9.

D. Distance between kicked minima

In Fig. 4(d) of the main text, we plot the normalized metric distance, as defined in Ref. [11], as a function of kick size for a system of 1024 particles. To obtain this data, we begin by selecting 13 random initial configurations. For each configuration, we use CVODE with `rtol` = 10^{-11} and `atol` = 10^{-12} (one order of magnitude below the values in Table S1) to locate the corresponding minimum within its basin of attraction. We only use jammed minima by discarding any fluid states and resampling.

For each of these 13 minima, we then apply 1000 random kicks of length R , choosing the direction uniformly in space, we do this for 60 R values. Of these 60 values, 10 are sampled uniformly in log space from 0.1 to 1 and 50 uniformly from 1 to $R = L$. In the main text, we only present the data up to $R = L/2$, confining ourselves to

observe differences in intermediate kick size regimes. After each kick, we minimize the system using CVMODE, FIRE, and L-BFGS, employing the parameters listed in Tables S1, S2, and S3, respectively. Finally, excluding any case in which the new minimum coincides with the original one, we compute the normalized metric distance between the new minimum M' and the original one M ,

$$d_{min}(M, M') \equiv \frac{1}{2\langle R_i \rangle} \sqrt{\sum_{i < j} (\mathbf{C}_{ij} - \mathbf{C}'_{ij})^2} \quad (\text{S16})$$

with $\langle R_i \rangle$ the average particle radius and $\mathbf{C}_{ij}, \mathbf{C}'_{ij}$ are the “stable contact vectors” between particles i and j in minima M and M' , respectively. These contact vectors are defined as

$$\mathbf{C}_{ij} = \mathbf{r}_{ij} \mathbb{1}(r_{ij} \leq R_i + R_j), \quad (\text{S17})$$

that is, the distance vector if the particles are in contact, and 0 otherwise. This definition ensures that the measured distance is unambiguous in spite of the presence of rattlers and of translational symmetry.

E. Basin volumes

To compute volumes of basins of attraction, we use the Markov Chain Monte Carlo method with umbrella sampling described in Refs. [8–10, 32], setting the “oracle” (the function that determines whether a point belongs to the basin being measured) to be either FIRE, L-BFGS, or CVMODE with the parameters described in Sec. IF. For each method, we compute the volume of 5 basins (the same ones across methods) at $\phi = 0.9$, across sizes ranging from $N = 16$ to $N = 128$. The choice $N = 128$ as the largest system size is due to the large computational cost of this method, as running the full procedure takes weeks for that system size on a full CPU node.

We here provide a list of the parameters we use for the various steps of the basin volume procedure. The minima used for basin volumes are found by sampling the size polydispersity (here bidisperse with half the radii positive-normal with mean and standard deviation $\mu_s = 1, \sigma_s = 0.05$ and the other half positive-normal with $\mu_\ell = 1.4$ and $\sigma_\ell = 0.07$), then sampling the locations of particle centers uniformly and independently in the simulation box, and identifying the corresponding basin it belongs to via a careful CVMODE minimization (10^7 optimization steps).

From that point, the algorithm is used with a choice of oracle that is kept constant throughout (either FIRE, L-BFGS, or CVMODE). The recorded minimum is re-quenched with that method to avoid possible small shifts of the minimum’s location due to, *e.g.* precision differences. When calling the oracle, we use as many as 10^5 optimization steps, and the method and tolerance value used for identification of the minimum are the ones described in Sec. IE, with a tolerance `dtol` = 10^{-4} . First, the largest spring constant k_{max} used in the umbrella sampling is found automatically as described in past work, by running a random walk biased by a spring attached to the minimum with an adjustable rigidity. The rigidity is adjusted, starting from $k_0 = 5/\mu_s^2$, until it reaches a value k_{max} such that 90% of samples lie in the basin. That proportion is evaluated using 10^4 samples per value of k . Then, we perform 10^5 steps of a free random walk within the basin ($k = 0$) so as to adjust the time step (to accept 20% of proposed MCMC steps on average) and measure an estimate of the extent of the basin, via the mean-square distance to the minimum of that walk. Parallel tempering is then performed using 64 replicas (40 positive ones, the $k = 0$ one, and the rest negative). The positive values of the stiffness constants are chosen such that the mode of their distributions of distances to the center are roughly linearly spaced between 0 and k_{max} , as described in Ref. [32], which ensures equivalent overlaps between neighboring histograms and good scaling of the required number of replicas with N . The negative replicas have linearly spaced k -values between $k = 0$ and $k = -0.5$, an arbitrary choice that empirically yields good behavior (meaning that the distance distribution of the most negative replica is not reduced to a point-like distribution and that histograms overlap sufficiently well). Replica exchanges are proposed every 10^2 steps. The Monte Carlo algorithm is run for a number of steps ranging from 5×10^5 to 2×10^6 steps, with a termination criterion based on an equilibration test [20]. To have a reference volume, we perform direct sampling of 10^5 independent points from a “radial Gaussian” [32] around the minimum, *i.e.* a distribution whose pdf of radial distances to the minimum $p(r)$ is a positive-Gaussian with a maximum at distance 0, corresponding to a high-dimensional pdf $p(\mathbf{r}) \propto r^{1-d} N(0, R_{in})$ for distance vectors to the minimum, where $N(\mu, \sigma)$ is the pdf of a normal distribution with mean μ and standard deviation σ . We choose the standard deviation R_{in} to match the mean root-square distance to the minimum in the k_{max} run. Each point thus sampled is kept only if it does fall into the basin, and we record the acceptance rate of the points to correct the integral of the reference volume. Finally, we reconstruct the volume of the basin using the pymbar implementation of MBAR [33]. As described in detail in Ref. [32], the method actually outputs the relative dimensionless “free energies” (negative log-volumes) $F(k_i)$ of each replica run, and the value of interest is obtained as the difference ΔF between the reconstructed free energy of a free walker $F_0 \equiv F(k = 0)$ and the known volume of the

radial Gaussian, corrected by the acceptance rate of the direct sampling, in units such that the simulation box volume is 1 (in other words, the reported volume is a fraction of the volume of configuration space). Results are reported as intensive free energies $F_0/N = -\log(v/\mathcal{V})^{1/N}$, with v the volume of the basin and \mathcal{V} the total volume of configuration space, that let us compare values across system sizes without the trivial scaling with N .

III. ADDITIONAL DATA

In this Section, we provide additional data that complements the results of the main text, but is not strictly necessary to arrive at the conclusions we draw.

A. Survival probability as a function of packing fraction

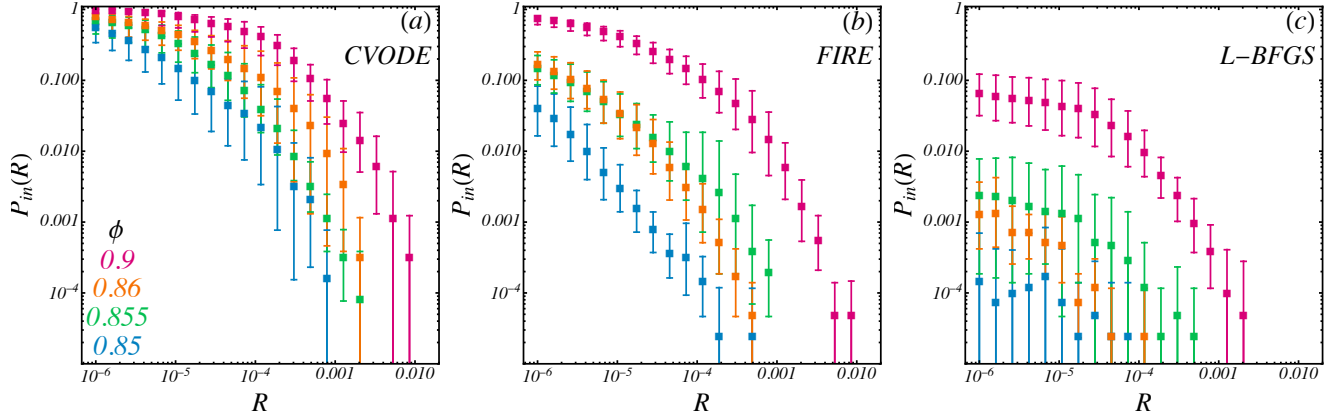


FIG. S4: **Survival: towards jamming.** Survival probability against kicksize for a few values of density, in log-log scales, getting closer to jamming, with (a) CVODE, (b) FIRE, and (c) L-BFGS. Error bars are Clopper-Pearson 95% confidence intervals.

In Fig. 4 of the main text, we report survival curves obtained across methods and at a couple of packing fractions for $N = 1024$ Hertzian disks. In this section, we report similar measurements across a wider range of densities. To obtain them, we use 13 random initial configurations for CVODE and 43 for FIRE and L-BFGS. We require more configurations for FIRE and L-BFGS because their survival probabilities are significantly lower and their variance is higher at the same error level. For each configuration, we provide 1000 uniform random kicks of length R for 30 different R , and measure the survival probability $P_{in}(R)$ as the fraction of points falling back to the same minimum. The results are shown in Fig. S4 for (a) CVODE, (b) FIRE, and (c) L-BFGS. We show that, as jamming is approached, the difference between methods becomes starker, as optimizers have a lower accuracy when ϕ approaches $\phi_J \approx 0.842$. In particular, optimizers approach power laws (straight lines in log-log) at densities as high as 0.85, for which CVODE retains a stretched-exponential-looking behavior with a clear characteristic lengthscale.

To quantify this behavior, we fit to two models. The first one is a stretched exponential,

$$P_{in}(R) = \exp\left(-\left(\frac{R}{R_{se}}\right)^\alpha\right) \quad (S18)$$

with R_{se} defining a characteristic lengthscale, and α a stretching exponent. The second one is a saturating power law

$$P_{in}(R) = \frac{A}{\left(1 + \frac{R}{R_{pl}}\right)^\beta} \quad (S19)$$

where A is a saturating factor, R_{pl} is a characteristic lengthscale, and β a power law exponent in the tail. To ensure that the fits accurately capture the tail, we perform weighted non-linear least-square fits in log space, with weights for each point r_i as $1/\delta_i^2$ where $\delta_i \equiv \Delta_i/P_{in}(r_i)$. Here Δ_i is the width of the 95% confidence interval on the observed point P_i . When the Central Limit Theorem applies, and the error can be assumed Gaussian, $\Delta_i \propto \sigma(r_i)$ where $\sigma(r_i)$

would be the variance at each point. To compare the fit quality, we compute the difference between the weighted residual sum of squares, ΔWRSS , defined as

$$\Delta\text{WRSS}_{\log} \equiv \text{WRSS}_{\text{power law}} - \text{WRSS}_{\text{stretched exp}} \quad (\text{S20})$$

as a function of ϕ . If the power law fit is better, $\Delta\text{WRSS}_{\log} < 0$ and if the stretched exponential fit is better, $\Delta\text{WRSS} > 0$. We then construct leave-one-out (or “jackknife” [34]) ensembles of the basins and find the proportion of the ensemble P_{pl} where $\Delta\text{WRSS}_{\log} < 0$, i.e the proportion where the data is better described by a power law, with 95% Clopper-Pearson confidence intervals. The resulting P_{pl} is plotted in Fig. S5 as a function of ϕ . We show that for L-BFGS, $P_{pl} \approx 1$ at all ϕ , suggesting power law behaviour at all packing fractions. For FIRE, $P_{pl} \approx 0$ at large ϕ , but becomes 1 close to jamming, suggesting an emergent power-law behaviour close to jamming. However, when using CVODE, we find that $P_{pl} < 0.5$ at all values of ϕ , and does not seem to grow nor decrease systematically with ϕ . In other words, CVODE reveals that the seemingly power-law behaviour of survival curves was yet another mirage linked to the use of inappropriate optimization methods.

For completeness, in Fig. S5(b)-(f), we report the values of the fitting parameters we found for each ϕ for both models (stretched exponential and power law), and across methods. We note in particular that the scale R_{se} of the stretched exponential fits with CVODE (Fig. S5(b), green symbols) remains nearly constant as jamming is approached, while the L-BFGS one for instance (blue symbols) becomes vanishingly small. This is an additional sign that basins are well-behaved shapes with finite length scales.

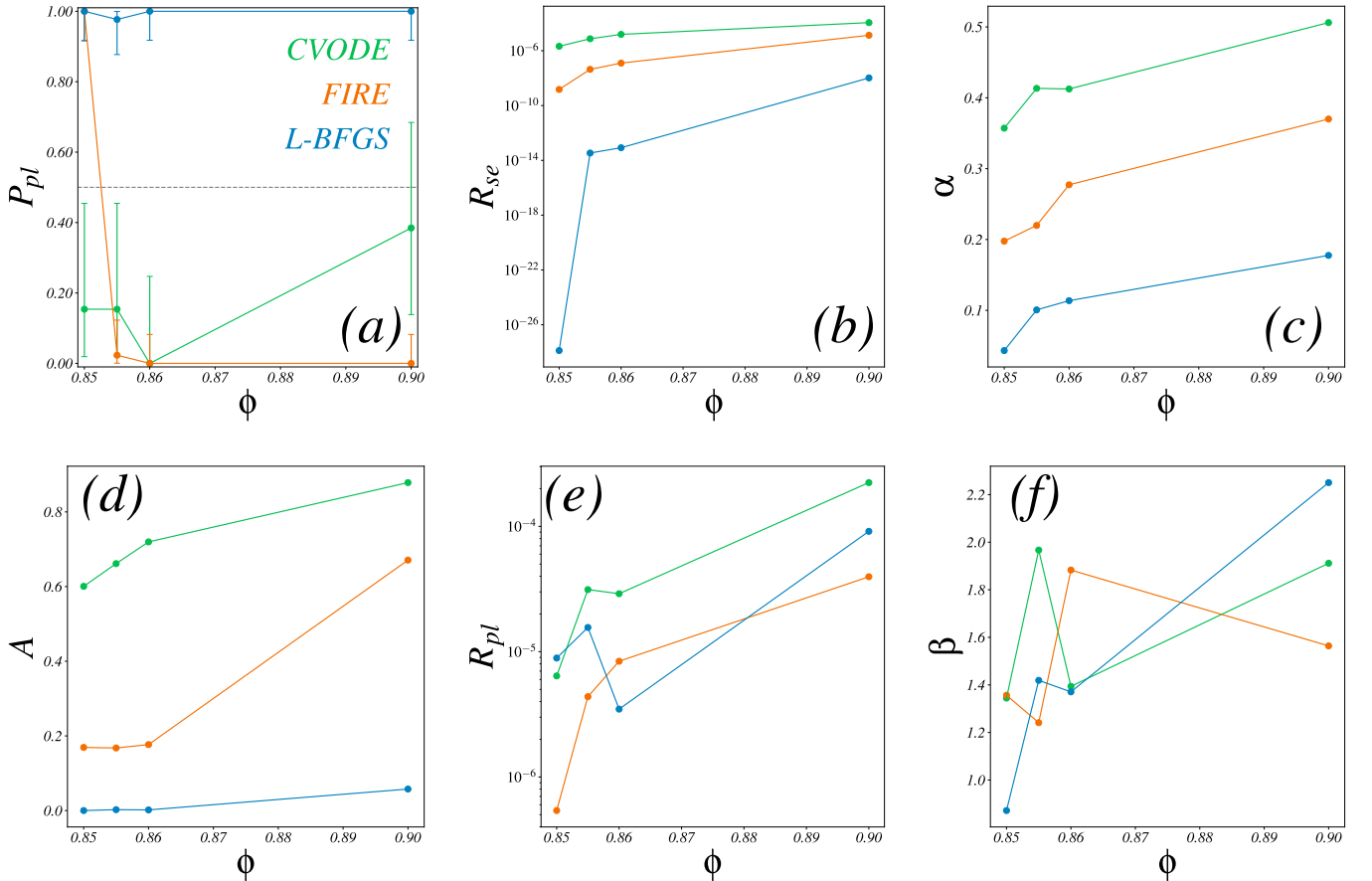


FIG. S5: **Survival: Fit Comparison** (a) Proportion P_{pl} of the leave-one-out ensembles for which the power law fit is better than the stretched exponential. Other panels show the values of the fitting parameters we found for each fitting function and method against ϕ , namely (b) R_{se} , (c) α , (d) A , (e) R_{pl} , and (f) β .

B. Jamming point

In this section, we present additional data on the location of the jamming transition as a function of system size and optimizer choice. We consider a few system sizes, $N = 8, 16, 32, 64, 128, 256, 512, 1024$ and, for each N , and a range of packing fractions $\phi \in [0.80; 0.86]$. For each (N, ϕ) combination, we draw a set of 10^3 random initial conditions uniformly in $[0; L]^{Nd}$, and perform relaxations from them using FIRE, L-BFGS, and CVODE to generate a list of minima (note that the figure in the appendix of the main text uses 10^4 points per density instead). We then measure the fraction P_J of these minima that is jammed, as per the criterion given in Sec. IE. The results are reported in Fig. S6. Across (a) CVODE, (b) FIRE, and (c) L-BFGS, P_J displays a finite-size transition from 0 at low ϕ to 1 at high ϕ , with a transition that gets sharper as N increases, as expected at jamming [35]. We show that using FIRE or L-BFGS leads to a systematic bias of the curve $P_J(\phi)$ towards lower values (fewer jammed states, more liquid states), meaning that ϕ_J is overestimated. However, this bias is most pronounced at small N , so that previous reports of ϕ_J values relying on large N or on N scalings were likely not noticeably affected by their choice of optimizer.

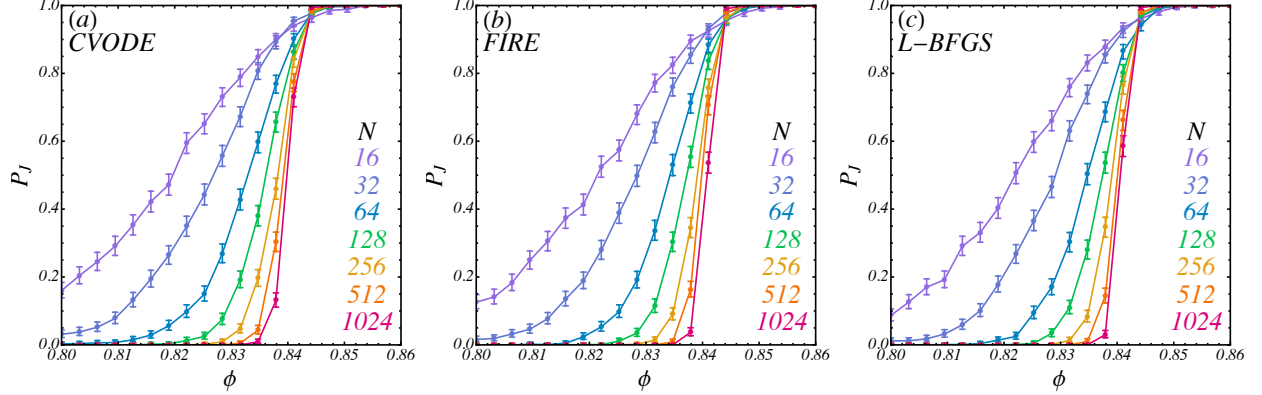


FIG. S6: **Jamming transition across sizes.** Fraction of jammed states as a function of packing fraction, across system sizes (color within panels), using (a) CVODE, (b) FIRE, and (c) L-BFGS. Error bars are Clopper-Pearson 95% confidence intervals.

To evaluate the jamming density presented in the main text, we perform a fit to a function of the form $P(\phi) = \sigma(ax + b)^p$ where $\sigma(x)$ is the sigmoid function, and we estimate a jamming packing fraction ϕ_J as the packing fraction at which $P_J = 1/2$. As mentioned in main text, we perform a finite-size scaling analysis of ϕ_J with N to assess the effect of the choice of method on critical properties. To do so, we collect $\phi_J(N)$ values and fit them, for each method, to a power law of the form $|\phi_J(N) - \phi_J^\infty| = CN^{-\theta}$ with fitting parameters ϕ_J^∞ the asymptotic ϕ_J , θ a critical exponent, and C a proportionality constant. We find that CVODE yields $\phi_{J(\text{CVODE})}^\infty \approx 0.8415$, whereas FIRE and CVODE yield $\phi_{J(\text{FIRE})}^\infty \approx 0.8423$, $\phi_{J(\text{LBFGS})}^\infty \approx 0.8422$ but slightly different exponents, $\theta_{\text{CVODE}} \approx 0.673$, $\theta_{\text{FIRE}} \approx 0.668$ and $\theta_{\text{LBFGS}} \approx 0.674$. These values are compatible with results from similar scaling analysis [35, 36]. We note that the probability of observing a jammed state is always higher with CVODE at all densities, as compared to using optimizer methods.

We further illustrate the effect of density on basins by reproducing the cuts from Fig. 2 of the main text at several ϕ , but using the same relative coordinates $\{\mathbf{r}_i/L\}_{i=1..N}$ and the same size polydispersity up to a global factor on all diameters, so that the slices correspond to the same initial point positions but different global dilations of the system. The results are shown in Fig. S7. In this figure, colors are *not* matched across slices as minima move across densities, and black indicate non-jammed (fluid) states. Going from $\phi = 0.828$ to $\phi = 0.86$, we show that the configuration space goes from being mostly made of fluid states and sparsely populated by basins to being tiled entirely by basins, at a packing fraction $\phi \approx 0.84$ comparable to the final plateau from Fig. S6 for $N = 128$.

Furthermore, the pictures show that the basins are all very slender at small densities, but become bulkier as density grows, highlighting the difficulties associated with both integrating steepest descent and measuring volumes at low densities. Interestingly, such slices taken at the same relative positions of configuration space display a sequential fragmentation of configuration space into basins as $\phi \rightarrow \phi_J^-$, reminiscent of thin sheet crumpling, see in particular illustrations in Ref. [37]. This suggests that the fragmentation of configuration space into basins as a function of density could be modeled by similar dynamical processes. Also note that the number of basins is maximal near jamming: as ϕ grows, for $\phi < \phi_J$, the liquid states get replaced by basins of jammed states, while for $\phi > \phi_J$ basins merge.

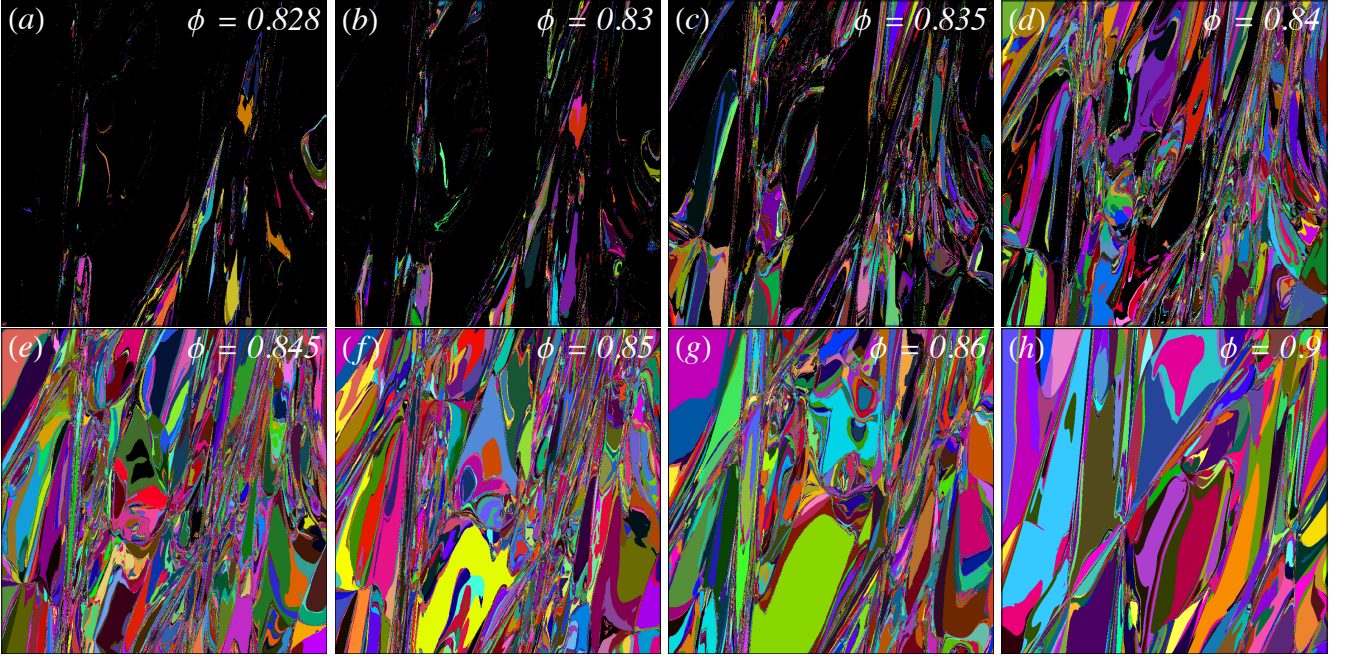


FIG. S7: **Density and landscape slices.** Slices of the energy landscape for $N = 128$ and at ϕ equal to (a) 0.828, (b) 0.830, (c) 0.835, (d) 0.84, (e) 0.845, (f) 0.85, (g) 0.86, (h) 0.9. Individual basins are encoded by colors, while liquid states are shown as black pixels.

C. Slices at $N = 8$

To complement the data shown in main text, in Fig. S8, we show a slice of the energy landscape of an $N = 8$ particle system at $\phi = 0.9$, measured using (a) CVODE, (b) FIRE, and (c) L-BFGS. Across these slices, identical minima are color-matched to highlight the error in basin tagging introduced by optimizers. Even at this very small N , at which the accuracies of FIRE and L-BFGS are fairly high (about 70% and 40%, respectively, as per Fig. 2 of the main text), there are noticeable basin deformations. Furthermore, as noted in several other parts of this paper, optimizers make basins look less regular, more “fractal-like”, even at modest N , in a way reminiscent of Refs. [3, 38].

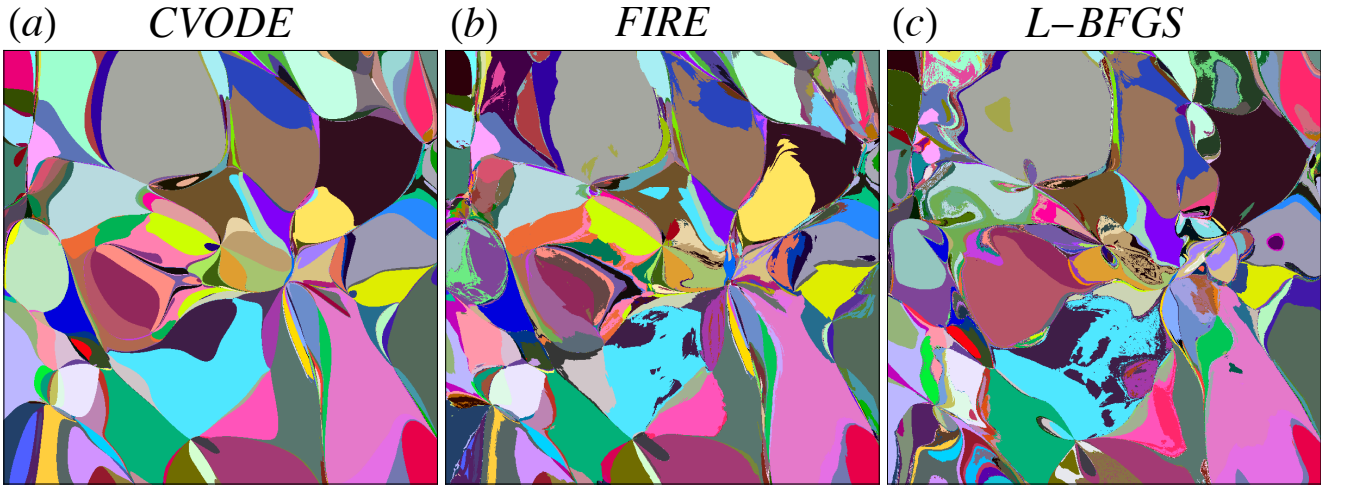


FIG. S8: **Small-system Slices.** Random $2d$ slice of the energy landscape of $N = 8$ particles at $\phi = 0.9$ using (a) CVODE, (b) FIRE, and (c) L-BFGS. Minima are matched across slices then color-coded.

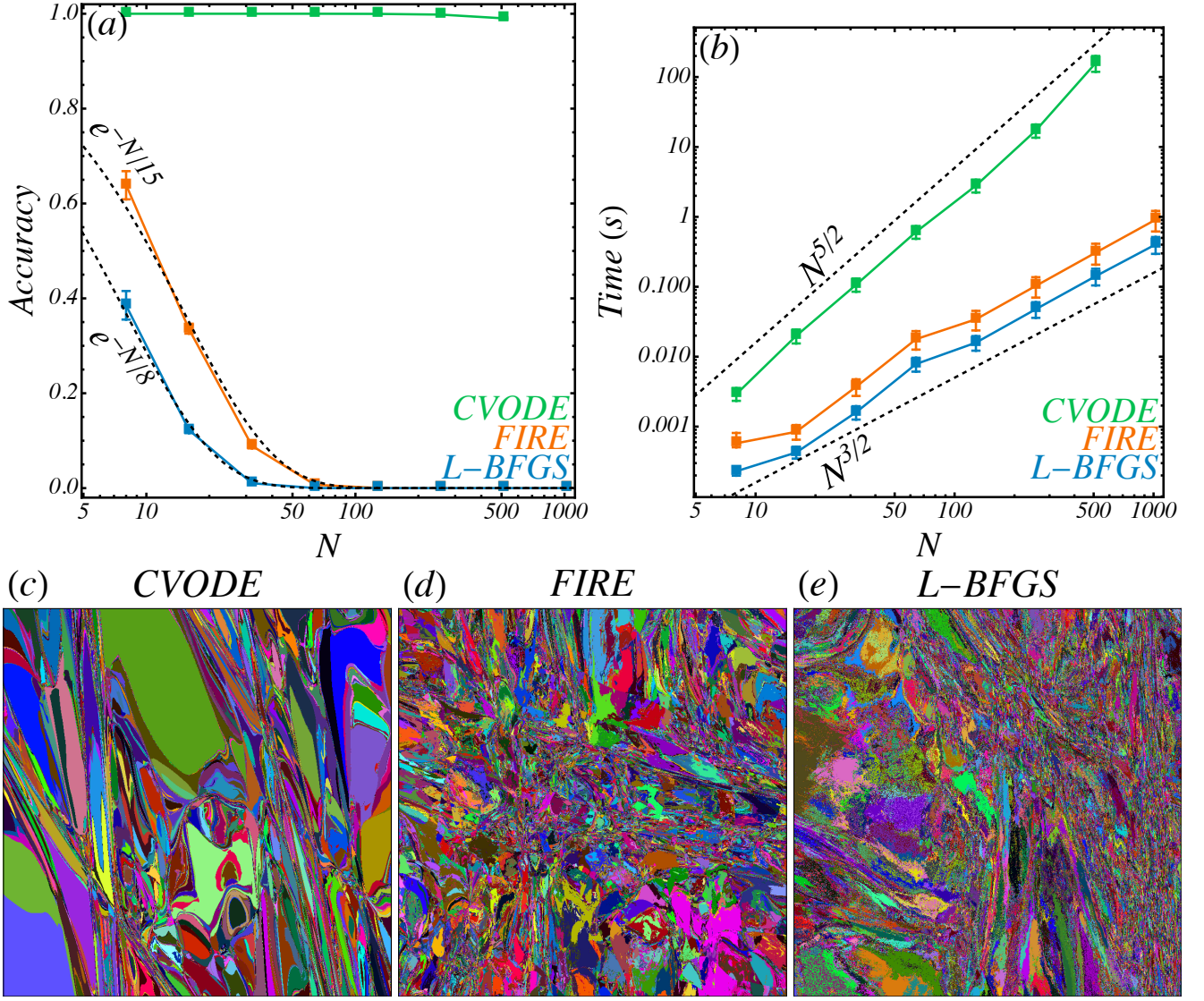


FIG. S9: **Optimizers: fast but inaccurate at every ϕ .** (a) Average accuracy of algorithms compared to low-tolerance CVODE, computed over 10^4 random uniform initial conditions. Error bars are 95% confidence intervals, obtained using a Clopper-Pearson estimator. Dashed lines are exponential fits, and the long-dashed line is a stretched exponential fit. (b) Corresponding scalings of the average computation times, with error bars obtained from a Student-T 95% confidence interval. (c) – (e) Like in Fig. 2 of the main text, we show 800×800 pixels slice for $N = 128$ particles for (c) CVODE, (d) FIRE, and (e) L-BFGS.

D. Accuracies and times at $\phi = 0.86$

In Fig. S9, we present results analogous to those of Fig. 2 of the main text, but at $\phi = 0.86$ and focus on optimizers compared to CVODE. We do not consider GD due to the much higher cost associated with it at large N . We show that (a) accuracies and (b) times follow the same trends as those presented at $\phi = 0.9$, namely exponentially decaying accuracies for optimizers, and time scalings $N^{3/2}$ for optimizers but $N^{5/2}$ for CVODE. Furthermore, landscape slices in Figs. S9(c) – (e) are qualitatively similar to those of the main text. In other words, the results of the main text are not specific to $\phi = 0.9$ but generic to the overcompressed regime of soft spheres.

E. Slices at $N = 128$

In in Fig. S10, we present additional slices of the energy landscape for $N = 128$ particles at $\phi = 0.9$, obtained for the same parameters as in Fig. 2 of the main text but with different random seeds.

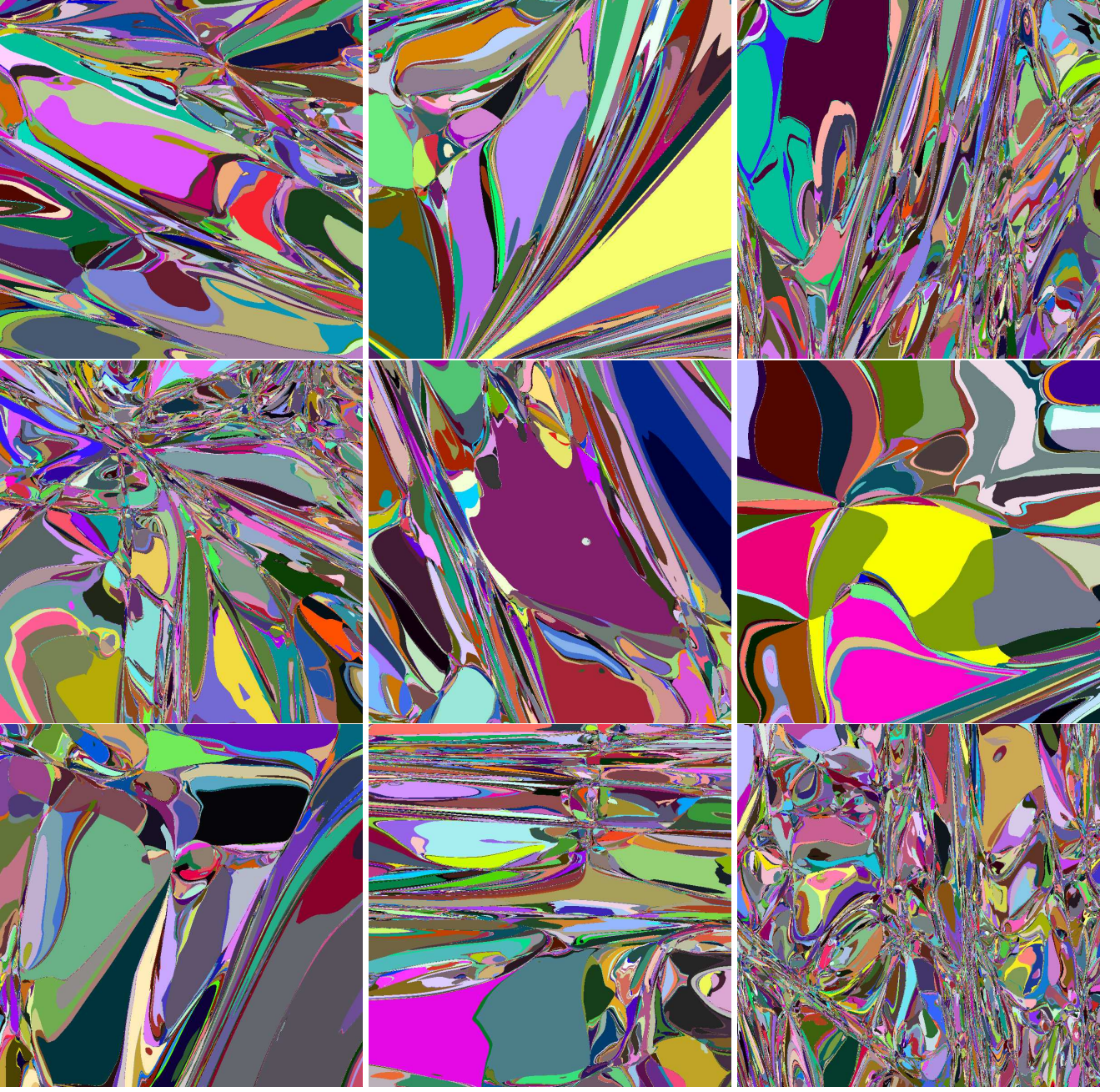


FIG. S10: **Gallery of energy landscape slices.** Slices of the landscape of $N = 128$ particles at $\phi = 0.9$, obtained for the same parameters as in Fig. 2 of the main text but with different random seeds.

[1] E. Hairer and G. Wanner, Solving ordinary differential equations. ii, vol. 14 of, Springer Series in Computational Mathematics (Springer Berlin Heidelberg, Berlin, Heidelberg, 1996) **10**, 978 (1996).

- [2] P. Charbonneau and P. K. Morse, Jamming, relaxation, and memory in a minimally structured glass former, *Physical Review E* **108**, 054102 (2023).
- [3] D. Asenjo, J. D. Stevenson, D. J. Wales, and D. Frenkel, Visualizing basins of attraction for different minimization algorithms, *Journal of Physical Chemistry B* **117**, 12717 (2013).
- [4] E. Stanifer and M. L. Manning, Avalanche dynamics in sheared athermal particle packings occurs via localized bursts predicted by unstable linear response, *Soft Matter* **18**, 2394 (2022).
- [5] N. Xu, D. Frenkel, and A. J. Liu, Direct determination of the size of basins of attraction of jammed solids, *Physical Review Letters* **106**, 245502 (2011).
- [6] C. Zhao, K. Tian, and N. Xu, New jamming scenario: From marginal jamming to deep jamming, *Physical review letters* **106**, 125503 (2011).
- [7] J. Nocedal and S. Wright, *Numerical Optimization* (Springer, 1999).
- [8] S. Martiniani, K. J. Schrenk, J. D. Stevenson, D. J. Wales, and D. Frenkel, Turning intractable counting into sampling: Computing the configurational entropy of three-dimensional jammed packings, *Physical Review E* **93**, 012906 (2016).
- [9] S. Martiniani, K. J. Schrenk, J. D. Stevenson, D. J. Wales, and D. Frenkel, Structural analysis of high-dimensional basins of attraction, *Physical Review E* **94**, 031301(R) (2016).
- [10] S. Martiniani, K. J. Schrenk, K. Ramola, B. Chakraborty, and D. Frenkel, Numerical test of the Edwards conjecture shows that all packings are equally probable at jamming, *Nature Physics* **13**, 848 (2017).
- [11] R. C. Dennis and E. I. Corwin, Jamming Energy Landscape is Hierarchical and Ultrametric, *Physical Review Letters* **124**, 78002 (2020).
- [12] V. F. Hagh and S. R. Nagel, Permutation Symmetry Restoration in Disordered Materials, *Arxiv Preprint*, 2403.03926 (2024), arXiv:2403.03926.
- [13] E. Bitzek, P. Koskinen, F. Gähler, M. Moseler, and P. Gumbsch, Structural relaxation made simple, *Physical Review Letters* **97**, 170201 (2006).
- [14] D. Asenjo, F. Paillusson, and D. Frenkel, Numerical calculation of granular entropy, *Physical Review Letters* **112**, 098002 (2014).
- [15] C. Rackauckas and Q. Nie, DifferentialEquations.jl – A Performant and Feature-Rich Ecosystem for Solving Differential Equations in Julia, *Journal of Open Research Software* **5**, 15 (2017).
- [16] A. C. Hindmarsh, P. N. Brown, K. E. Grant, S. L. Lee, R. Serban, D. E. Shumaker, and C. S. Woodward, SUNDIALS: Suite of nonlinear and differential/algebraic equation solvers, *ACM Transactions on Mathematical Software* **31**, 363 (2005).
- [17] D. J. Gardner, D. R. Reynolds, C. S. Woodward, and C. J. Balos, Enabling New Flexibility in the SUNDIALS Suite of Nonlinear and Differential/Algebraic Equation Solvers, *ACM Transactions on Mathematical Software* **48**, 31 (2022).
- [18] J. M. Kosterlitz, The critical properties of the two-dimensional $\{XY\}$ model, *Journal of Physics C: Solid State Physics* **7**, 1046 (1974).
- [19] D. A. Wiley, S. H. Strogatz, and M. Girvan, The size of the sync basin, *Chaos* **16**, 015103 (2006).
- [20] S. Martiniani, *On the complexity of energy landscapes: algorithms and a direct test of the Edwards conjecture*, Ph.D. thesis (2017).
- [21] Y. Zhang and S. H. Strogatz, Basins with tentacles, *Physical Review Letters* **127**, 194101 (2021).
- [22] Y. Zhang, P. S. Skardal, F. Battiston, G. Petri, and M. Lucas, Deeper but smaller: Higher-order interactions increase linear stability but shrink basins, *Science Advances* **10**, eado8049 (2024).
- [23] J. Villain, Spin glass with non-random interactions, *Journal of Physics C: Solid State Physics* **10**, 1717 (1977).
- [24] J. Villain, Two-level systems in a spin-glass model. I. General formalism and two-dimensional model, *Journal of Physics C: Solid State Physics* **10**, 4793 (1977).
- [25] J. Lee, J. M. Kosterlitz, and E. Granato, Monte Carlo Study of Frustrated XY Models on a Triangular and Square Lattice, *Physical Review B* **43**, 11531 (1991).
- [26] C. Tsitouras, Runge–kutta pairs of order 5 (4) satisfying only the first column simplifying assumption, *Computers & Mathematics with Applications* **62**, 770 (2011).
- [27] Y. Saad and M. H. Schultz, GMRES: a generalized minimal residual algorithm for solving nonsymmetric linear, *SIAM Journal on Scientific Statistical Computing* **7**, 856 (1986).
- [28] J. D. Stevenson, S. Martiniani, and J. Schrenk, *pele* (2024).
- [29] C. Glasbey, G. van der Heijden, V. F. Toh, and A. Gray, Colour displays for categorical images, *Color Research & Application: Endorsed by Inter-Society Color Council, The Colour Group (Great Britain), Canadian Society for Color, Color Science Association of Japan, Dutch Society for the Study of Color, The Swedish Colour Centre Foundation, Colour Society of Australia, Centre Français de la Couleur* **32**, 304 (2007).
- [30] J. Gostick, Z. Khan, T. Tranter, M. Kok, M. Agnaou, M. Sadeghi, and R. Jervis, PoreSpy: A Python Toolkit for Quantitative Analysis of Porous Media Images, *Journal of Open Source Software* **4**, 1296 (2019).
- [31] G. Folena, P. Charbonneau, P. K. Morse, R. D. H. Rojas, and F. Ricci-Tersenghi, Jamming the Random Lorentz Gas: Configurational Entropy, Crunching Geometry, and Critical Universality, *Arxiv Preprint*, 2410.05784 (2024).
- [32] M. Casiulis and S. Martiniani, When you can't count, sample! Computable entropies beyond equilibrium from basin volumes, *Papers in Physics* **15**, 150001 (2023).
- [33] M. R. Shirts and J. D. Chodera, Statistically optimal analysis of samples from multiple equilibrium states, *Journal of Chemical Physics* **129** (2008).
- [34] B. Efron, Bootstrap methods: another look at the jackknife, *Annals of Statistics* **7**, 1 (1979).
- [35] C. S. O'Hern, L. E. Silbert, A. J. Liu, and S. R. Nagel, Jamming at zero temperature and zero applied stress: The epitome of disorder, *Physical Review E - Statistical Physics, Plasmas, Fluids, and Related Interdisciplinary Topics* **68**, 011306 (2003).

- (2003).
- [36] D. Vågberg, D. Valdez-Balderas, M. A. Moore, P. Olsson, and S. Teitel, Finite-size scaling at the jamming transition: Corrections to scaling and the correlation-length critical exponent, *Physical Review E - Statistical, Nonlinear, and Soft Matter Physics* **83**, 030303(R) (2011).
 - [37] J. Andrejevic, L. M. Lee, S. M. Rubinstein, and C. H. Rycroft, A model for the fragmentation kinetics of crumpled thin sheets, *Nature Communications* **12**, 1470 (2021), arXiv:2005.12369.
 - [38] D. J. Wales, Basins of Attraction for Stationary Points on a Potential-Energy Surface, *Journal of the Chemical Society: Faraday Transactions* **88**, 653 (1992).